Delft University of Technology
Faculty of Civil Engineering and Geosciences

# The Dynamic Response of a Hyperloop Tube

December 14, 2024

**Graduation candidate**

| | |
|---|---|
| Dennis Kuiper, 5851068 | Structural Engineering |

**Graduation committee**

| | |
|---|---|
| K.N. van Dalen (chairman) | Dynamics of Structures |
| R.J. van Leijden (daily supervisor) | Dynamics of Structures |
| I.B.C.M. Rocha | Applied Mechanics |
| A.B. Faragau | Dynamics of Structures |
| S.J.H. Meijers | Royal HasKoningDHV |
| R.F. Vorderegger | Royal HasKoningDHV |


Master Thesis - academic year 2024/2025

# Abstract

The Hyperloop concept tackles the challenges conventional transport modes face, despite the considerable research gap. This research reduces the gap by focusing on the dynamic response of the periodically supported Hyperloop tube since the Hyperloop greatly exceeds the operational speed of traditional transport modes. Complexity is incorporated to obtain a detailed dynamic response using a finite element method. Progress has been made in incorporating the moving reference frame within the model with recommendations for the numerical stability of the transient analyses. Despite the computational inefficiency of the conventional non-moving reference frame, the model is utilised to conduct a parametric study. The study examines correlations between the stiffness properties of various Hyperloop elements, including the tube, rail, and the interface between the Hyperloop tube and column. These correlations are analyzed based on the system's response at the pod's location and the intersections between the tube segments. Here, the velocity of the pod is of paramount importance. Within the operational velocity range, only one critical velocity is identified, despite the system's infinite number of natural frequencies. The only dynamic amplification, identified as the main critical velocity, can be shifted beyond the operational range by increasing the overall structural stiffness. The shift can be realised due to the positive correlation with the main critical velocity and a negative correlation with the displacement difference at the interface between two tube segments relative to the structural stiffness. Within the research, the soil and pod interactions with the Hyperloop structure are excluded, leading to potential resonance with no risk of instability. The limitation can be addressed by modelling the pod as a mass-spring system and the soil as a two-dimensional medium. The files developed for the finite element models and the parametric study are available on GitHub [1]. The files support reproducibility and further exploration of the methods described.

# Contents

# List of Figures

# 1 | Introduction

## 1.1 Background

Due to an increase in the population and the need to travel, the transport system reaches its limits. Over time, the system will be overloaded and the comfort of the passengers decrease drastically therefore an expansion is needed. Contemporary conventional transport modes are expanded resulting in several problems. The biggest problems that have to be faced are the use of limited space and being environmentally friendly. Additionally, the current modes can be optimized to improve other factors like safety, comfort, capacity and travel time. Unfortunately, the modes have reached their potential and with the current modes, the transport system is difficult to make resilient and future-proof [4].

The concept of the Hyperloop is a very promising unconventional transport mode. The Hyperloop is a transport mode with pods moving through a low-pressure tube. By significantly reducing air resistance and friction, the Hyperloop enables pods to travel up to a velocity of 1000 km/h. The two key principles of the system are the magnetic levitation of the pod and the near-vacuum environment, reducing the rolling and air resistance significantly. The new transport tackles the problems of the conventional modes and offers numerous advantages, which are shown in Figure 1.1. The claims in the figure are not rigorously researched and should not be taken for granted. To realise the Hyperloop a lot of research has still to be conducted. Many companies have been built to create the Hyperloop system in the future since Elon Musk ensured a kickstart in 2015 with a Hyperloop pod design competition in 2015 [5]. In the last decennia, research has been done on all aspects of the new concept from the vehicle and operational system to the infrastructure and its support structure with promising results [6]. However since the concept can still be considered quite new, a lot still has to be uncovered on all levels. Looking through the eyes of a Civil engineer, the support structure must be investigated thoroughly because the effects of vehicles passing by on the structure and the surroundings are still unclear. A detailed discussion of the existing literature is provided in Section 2.


Figure 1.1: Benefits of hyperloop [2]

## 1.2 Research Objectives and Questions

This research aims to build the finite element model in a moving reference frame and get a better perception of the dynamic response of the Hyperloop tube induced by the travelling pod. The moving reference frame is not researched intensely for moving load problems. However, these problems do not encounter pod velocities of 1000 km/h. Existing models focus only on beams supported by a continuous and periodic foundation, with no models addressing other periodicities within the system, such as the rail supports. Most researchers still rely on the conventional non-moving reference frame, covering the basic concepts of the Hyperloop. This research seeks to advance the field by incorporating additional Hyperloop characteristics into the finite element model to get a better perception of the dynamic response. This response can be visualised by the displacement difference at a tube intersection and vertical displacement below the pod. The research objective is translated into questions. Throughout the thesis, the following research questions will be answered:

- To what extent is a moving reference frame feasible for a moving load problem within a finite element model?
  - How does a moving reference frame influence the accuracy and computational efficiency for a moving load problem within a finite element model?
  - What are the key considerations for a stable implementation of a moving reference frame model for a moving load problem within a finite element model?
- What is the influence of the system's parameters on the dynamic response of the Hyperloop tube?
  - What is the influence of the pod's velocity and the different element stiffnesses on the vertical displacement of the tube below the moving pod?
  - What is the influence of different element stiffnesses on the displacement difference at a tube intersection?
  - What is the influence of different soil implementation types for Dutch soil in a periodic supported model?

## 1.3 Research Approach

This research will give insights into the Hyperloop tube's dynamic response under ultra-high speeds utilizing a simulation model. The model is based on Finite Element Method (FEM) and set in a moving reference frame. The domain will be discretized with the weighted residual method without the use of existing FEM software. The model utilises the programming language 'Python' with only its standard packages Numpy, Scipy and Matplotlib. The initial code is a simple model developed within a non-moving reference frame to align with existing research. The next step involves translating the model into a moving reference frame. The moving reference frame is used to overcome extensive computation time due to the potential reduction in the domain size. When the simple moving reference frame model is validated, the model can be expanded into the desired FEM model by adding several different components. The desired model provides a more detailed representation of the Hyperloop system, which adversely impacts computational time. The model will be built in a two-dimensional space domain, taking into account only the vertical displacement and rotation. The dynamic response is examined in a parametric study by investigating the sensitivity of the structure's parameters. The study focuses on the vertical displacement of the tube below the pod and the displacement difference at the tube intersection. The external parameters of the soil will be considered with a literature study about the important parameters influencing the dynamic response. The limitations of the model are addressed in Section 7.2.

# 2 | Literature Review

The Hyperloop is a promising concept for transportation in the future. Before realisation, a lot of research has to be done to ensure the bright advantages can be met and safety can be assured. Since Elon Musk launched his Hyperloop project in 2013 [5], companies and academic institutions have been built gaining momentum to take up the challenge. Delft is well represented with the startup Hardt Hyperloop and Delft Hyperloop, the program facilitated by the TU Delft. The focus of the research has been mostly on aerodynamics and electromagnetic technologies since these aspects create a whole new research area [6]. Consequently, the structural aspect has less priority but has to overcome its own difficulties, both statically and dynamically. The ultra-high-speed within the Hyperloop system, approximately 1000 km/h, introduces a range of dynamic responses that have not been observed in generic high-speed trains [7][8]. These articles focus on the vibrations and wave propagations in the supporting structure under an ultra-high-speed load and cover the basis of the concept but do not address the critical velocities of the Hyperloop system. Only Fărăgău and Lu investigated the critical speeds for moving loads with an ultra-high-speed [9][10][11]. The pod running through the tube is represented by a moving load. Railway engineers are already researching structures impacted by a moving load for a long time. They investigate the dynamic response and wave propagation phenomena. The vibrations may become large when the moving load velocity approaches a certain critical velocity [12]. The critical velocities need to be identified to prevent the velocities from occurring in operational regions. The periodic supports play a great role in the critical velocities [13][14]. Railway engineers experience already critical cases due to the periodic placing of sleepers and rail segments.

## 2.1 Finite-Element Method

The Hyperloop system can be represented in several ways with its pros and cons. Lu describes the model as semi-analytical with an infinite Euler-Bernoulli beam subjected to a moving load with a constant magnitude. The beam is supported periodically with springs and dashpots to represent the supports of the tube and investigated analytically with Vostroukhov's and Metrikine's procedure [13]. The model is a simplification of reality. Lu's model lacks some periodic supports of the tube. The suspension of the rail and the sequence rail segments for thermal expansion are also periodic. By adding the periodic supports, the dynamic response will increase in accuracy. However, running time and complexity will increase significantly as well. The semi-analytical modelling approach is appropriate for simplistic models with a smaller domain than a numerical analysis due to the matching periodic boundaries. By contrast, extensive models are difficult to implement, if not impossible. A numerical analysis could be favourable for a detailed model.

Several other techniques can be used to obtain the approximate solution of higher-order partial differential equations (PDEs). The finite element method (FEM) suits the best for this specific case. The method is easy to understand and apply as well as the finite difference method (FDM). However in comparison with FDM, FEM is suited better for problems with complex geometries and is easier to write general-purpose computer codes for FEM formulations [15]. FEM is a numerical approach that discretises the domain in space represented by a set of element equations which are systematically recombined into the global system of equations. The method is easily adjustable and could represent complex structures well.

## 2.2 Model Elements

The Hyperloop system can be modelled by an Euler-Bernoulli beam subjected by a moving load with an ultra-high speed periodically supported by spring-dashpot systems. The equation of motion of the Euler-Bernoulli beam reads:

$$m\ddot{u} + EIu'''' + c\dot{u} + ku = f \tag{2.1}$$

With $EI$ being the bending stiffness, $m$ being the mass, $f$ beining the acting force [N] and $c$ and $k$ being extra damping and stiffness terms. The stiffness term is used to represent a continuous support, together with the damping term. In addition, the damping is used for the absorbing layer explained in Section 2.5. The Euler-Bernouli beam makes use of the classical beam theory and is simple and efficient, but has also its limitations. No shear deformation, rotational inertia and nonlinearity are included. Therefore, the theory describes the behaviour of slender, linear elastic beams with small deflections. For other beams, an advanced theory like the Timoshenko beam theory is more suitable since the theory accounts for shear deformation and rotational inertia [16]. The springs in the model are a simplification of reality and are used to store, absorb and release energy over time with the following equation of motion:

$$k_{spring} \cdot u = f \tag{2.2}$$

No mass is included, only a stiffness ($k_{spring}$) is added to the mechanical system [17]. For rotational springs, the equation of motion is slightly different: instead of $u$ the first derivative of $u$ ($\dot{u}$) to space is multiplied by $k_{spring}$ to give resistance to the angle instead of the displacement. The dashpots have been added to the system to include damping. The equation of motion of the dashpot reads:

$$c_{spring} \cdot \dot{u} = f \tag{2.3}$$

The damping ($c_{spring}$) makes the model more realistic and stable. The function is to dissipate energy over time to control the dynamic response and improve numerical stability. In reality, energy is also released out of the system due to friction [18].

## 2.3 Weighted Residual Method

The weighted residual method transforms the continuous equation of motions into discrete systems of algebraic equations:

$$u(x) \approx \underbrace{\begin{bmatrix} N_1(x) & N_2(x) & N_3(x) & N_4(x) \end{bmatrix}}_{\mathbf{N}(x)} \begin{bmatrix} u_l \\ \theta_l \\ u_r \\ \theta_r \end{bmatrix} = \mathbf{N}(x)\mathbf{u} \tag{2.4}$$

The method formulates the FEM problem and obtains the approximate solution to the differential equation. The unknowns are approximated by trial functions that satisfy the boundary conditions. The calculation of the trial functions for this research are shown in Appendix A. The assumed solution is substituted in the differential equation. The solution is an approximation, resulting in a deviation of the exact solution called residual ($R_\mathrm{s}$):

$$m\mathbf{N}(x)\ddot{\mathbf{u}} + EI\mathbf{N}''''(x)\mathbf{u} - f(x) = \underbrace{R_\mathrm{s}(x)}_{\neq 0} \tag{2.5}$$

The residual function shows the difference between the actual and predicted values and will be zero when the approximated unknowns out of Equation 2.4 match the exact solution. The residuals are forced to be zero in an average sense by setting weighted integrals of the residuals to zero with the target to approach the exact solution. The integral helps to spread the possible error and to cancel out the residual over the domain. In addition, the integral operation can reduce the order of continuity on the approximate function via integration by parts. The equation can be altered by changing the weighted functions and/or the trial functions to find the best approximated solutions.

$$\int_0^L W_i(x) R_\mathrm{s}(x)\, dx = 0 \tag{2.6}$$

The integral is called the weak form and weakens the continuity on the approximate function shown in Equation 2.4. The performance of the method depends on the selected weight functions. Several methods are used to derive the best weight function. This research focuses on the Galerkin and least square method.

**Galerkin Method**

The Galerkin method [19] is widely used in numerical methods due to its easy implementation and low computational effort compared to other methods, especially in FEM. The method makes use of the trial functions as the weighted functions, resulting in a symmetric system matrix for the non-moving reference frame model, resulting in the weighted residual function below:

$$W_i(x) = N_i(x) \quad \text{for} \quad i = 1, 2, 3, 4 \tag{2.7}$$

$$\int_0^L \mathbf{N}(\mathbf{x})^T R_{\mathrm{s}}(x) dx = 0 \tag{2.8}$$

The integral has to be worked out to end up in the form below:

$$\mathbf{M} \begin{bmatrix} \ddot{u}_l \\ \ddot{\theta}_l \\ \ddot{u}_r \\ \ddot{\theta}_r \end{bmatrix} + \mathbf{C} \begin{bmatrix} \dot{u}_l \\ \dot{\theta}_l \\ \dot{u}_r \\ \dot{\theta}_r \end{bmatrix} + \mathbf{K} \begin{bmatrix} u_l \\ \theta_l \\ u_r \\ \theta_r \end{bmatrix} = f \tag{2.9}$$

The whole calculation is added to Appendix A with the values in the mass, damping and stiffness matrix. Unfortunately, a moving reference frame does not have a symmetric system matrix. The velocity of the moving load will be present in stiffness matrices and makes them non-symmetrical, resulting in a less stable system. The velocity of the moving load is incorporated into the stiffness matrices, making the matrices non-symmetrical, leading to a less stable system. Anderson already had established that instability may occur due to the negative numerical damping if standard Galerkin's approach is applied [20]. For velocities far below the critical velocity, adding physical damping could prevent the instability. When the model runs at operational speed ($300 m/s$), the method causes instability. Dai suggests using Petrov–Galerkin or Taylor–Galerkin approaches [21]. Froio makes use of the least squares finite element method to overcome numerical instabilities [22].

**Least squares method**

In the least squares method, a mixed formulation is included. The equation of motion of the Euler-Bernoulli beam is divided into two equations of motion to improve accuracy and stability [23]. The formulation addresses complex interaction without inducing numerical issues like shear locking. The higher order derivatives in space are removed by substituting the displacements to the 2nd and 4th order of space by the moment. The Equation below gives the mixed formulation for the equation of motion shown in Equation 2.1.

$$\begin{cases} -\mathbf{M}'' + m\left(\frac{V^2}{EI}\mathbf{M} - 2V\dot{\mathbf{u}}' + \ddot{\mathbf{u}}\right) + c(r)\left(\dot{\mathbf{u}} - V\mathbf{u}'\right) + k\mathbf{u} = \mathbf{F}_{\mathbf{r}}\delta(0) \\ \mathbf{M} + EI\mathbf{u}'' = 0 \end{cases} \tag{2.10}$$

The basic idea behind the residual computation of the least squares method is the approximation of the variables of each equation with the sum of the squares of the residuals constructs the integral statement [24]. The least squares method minimize the integral with respect to the unknown parameters of the approximations and gives a weight function that can be substituted in Equation 2.6.

$$W_i(x) = \frac{\partial(R_s)}{\partial \alpha_i} \quad \text{for} \quad i = 1, 2, 3, 4 \tag{2.11}$$

$$\int_0^L \frac{\partial(R_s)}{\partial \alpha_i} R_{\mathrm{s}}(x)\, dx = 0 \quad \text{for} \quad i = 1, 2, 3, 4 \tag{2.12}$$

The integral is put in Maple to find the local matrices. The elaborated calculation resulting in the local matrix is shown in Appendix B. The key parameters integrated into the matrix include the element size ($l$), the velocity of the moving load ($V$), the damping ($c$) and stiffness ($k$) of the distributed foundation and the bending stiffness ($EI$) and mass ($m$) of the Euler-Bernoulli beam.

## 2.4 Newmark Method

The system of equations derived from the weighted residual method can be solved and give the displacements per defined nodes. All equations are linear and can be calculated with a direct integration method despite the dynamic problem which contains first and second derivatives as can be seen in Equation 2.1. The most commonly used direct integration method is the Newmark Method because the method is implicit and unconditionally stable for specific parameters ($\gamma = \frac{1}{2}$; $\beta = \frac{1}{4}$), called Constant-Average-Accelerations [25]. The Newmark method is an explicit analysis, resulting in no influence of the Courant number. For an explicit analysis, the Courant number must be smaller than 1 since an explicit time integration is applied to the phase fraction [26]. The Courant number in Equation 2.13 shows the number of finite elements that are skipped by the moving load per time step. Therefore, the Newmark method can facilitate larger time steps and lower computation time.

$$Courantnumber = \frac{V\Delta t}{\Delta x} \tag{2.13}$$

The Newmark Method discretizes time and calculates per time step the unknowns by multiplying the inverse of the stiffness matrix and the force vector. For dynamic problems, the inverse of the effective stiffness matrix is used to take into account the mass and damping matrix with defined factors. The force vector is updated at each time step due to the moving load and an effective force vector is calculated using the Mass and Damping matrix again [27].

$$\Delta\mathbf{u} = \mathbf{u}_{t+\Delta t} - \mathbf{u}_t \tag{2.14}$$

$$\mathbf{K}_{\text{eff}} \cdot \mathbf{u} = \mathbf{F}_{\text{eff}} \tag{2.15}$$

$$\mathbf{K}_{\text{eff}} = \left(\frac{1}{\beta\,\Delta t^2}\right)\mathbf{M} + \left(\frac{\gamma}{\beta\,\Delta t}\right)\mathbf{C} + \mathbf{K} \tag{2.16}$$

$$\begin{aligned}\mathbf{F}_{\text{eff}} = \mathbf{F} &+ \mathbf{M}\left(\left(\frac{1}{\beta\,\Delta t^2}\right)\mathbf{u}_t + \left(\frac{1}{\beta\,\Delta t}\right)\mathbf{v}_t + \left(\frac{1}{2\beta} - 1\right)\mathbf{a}_t\right) \\ &+ \mathbf{C}\left(\left(\frac{\gamma}{\beta\,\Delta t}\right)\mathbf{u}_t + \left(\frac{\gamma}{\beta} - 1\right)\mathbf{v}_t + \Delta t\left(\frac{\gamma}{2\beta} - 1\right)\mathbf{a}_t\right)\end{aligned} \tag{2.17}$$

Equation 2.15 can be rewritten to isolate the displacements by taking the inverse of the effective stiffness matrix.

$$\mathbf{u}_{t+\Delta t} = K_{\text{eff}}^{-1} \cdot F_{\text{eff}} \tag{2.18}$$

$$\mathbf{a}_{t+\Delta t} = \left(\frac{1}{\beta\,\Delta t^2}\right)\Delta\mathbf{u} - \left(\frac{1}{\beta\,\Delta t}\right)\mathbf{v}_t - \left(\frac{1}{2\beta} - 1\right)\mathbf{a}_t \tag{2.19}$$

$$\mathbf{v}_{t+\Delta t} = \mathbf{v}_t + (\Delta t\,(1-\gamma))\,\mathbf{a}_t + (\gamma\,\Delta t)\,\mathbf{a}_{t+\Delta t} \tag{2.20}$$

## 2.5 Absorbing Boundary Layer

The absorbing boundaries damp out propagating waves coming into the boundary layer. The reflections of the propagating waves must be attenuated before leaving the boundary layer again. Therefore, a closer look is taken at the origin of the waves. The propagating waves can occur in the Euler-Bernoulli beams travelling along the length and are governed by the beam's properties and the angular frequency of the wave, resulting in frequency-dependent waves. This research takes place in the time domain with a transient analysis, meaning the frequency is difficult to grasp and determine despite the important influence.

The domain can be increased sufficiently large to damp out the waves, resulting in a large computation time. The absorbing boundary layers can be seen as a catalyst to damp out the propagating waves. The layers reduce the domain size significantly and overcome the computational inefficiency. The layers include viscous damping in a manner that all incident waves should be absorbed [28]. The closer to the boundary the larger the artificial damping will be as can be seen in the equation below:

$$c(x) = \begin{cases} c & \text{if } |x| < L_0, \\ c + \eta \left( \frac{|x| - L_0}{\delta} \right)^4 & \text{if } |x| > L_0, \end{cases} \tag{2.21}$$

Where $L_0$ is half of the interested domain and $\delta$ is the width of the absorbing boundary layer. The parameters $c$ and $\eta$ are constant and respectively the standard damping in the interested domain and the additional damping added in the boundary layer. The values of $\eta$ and $\delta$ are derived by trial and error with the focus on damping the propagating waves with the smallest domain, while the damping within the absorbing layer is strong enough to effectively attenuate outgoing waves and the variation of damping across the absorbing layer is sufficiently smooth to prevent reflection waves in between the finite elements due to abrupt changes in damping. When the layers are built correctly, the displacement and rotation in the last nodes of the domain are already almost zero. Resulting in almost no influence of the type of boundary condition (free or fixed) at the end of the layers.

## 2.6 Instability

Throughout this research, the term 'instability' refers specifically to numerical instability within the Finite Element Model (FEM). Numerical instability arises due to improper choices in the FEM setup. Potential causes of numerical instability within this model will be analyzed, including mesh refinement issues, method selection, element selection, time-stepping algorithms and the treatment of boundary conditions. These factors are critical to ensure the model represents the physical behaviour of the system accurately. Requires careful refinement of the mesh, time integration scheme and the choice of the damping parameters to ensure convergence and reliable results.

Numerical instability is the only instability occurring in this research due to the use of a moving constant load. Despite the dynamics, no dynamic instability occurs. For dynamic instability, the load has to vary with time or interact with the natural frequency of the system applying to more loading scenarios such as a rapidly changing force or a mass-spring system that has coupling. In these cases, the model may struggle to converge and show the behaviour correctly independent of the time step and element size.

# 3 | Non Moving Reference Frame Model

## 3.1 Model Description

The aim of the Python model is to try to match the phenomena occurring in reality the best as possible. The degree of model complexity has to be determined based on the aims of the research. A detailed model approaches reality better but has a higher computation time as a trade-off. In addition, the relations of important factors on the response are difficult to isolate due to more included depending factors. Therefore, the model starts simplistic and becomes more detailed step by step. From an Euler-Bernoulli beam on an elastic foundation to the schematic model shown below.

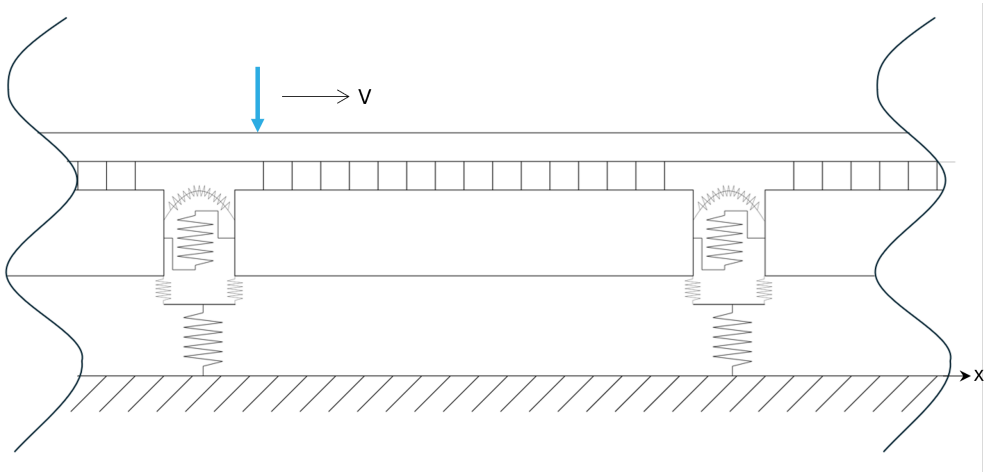


Figure 3.1: Schematic representation of the Finite-Element Model

The final model has a constant load moving with a specified velocity over the rail. The model makes use of two types of elements: beams (Rail within the tube; Tube segments) and spring-dashpot systems (Columns; Bearings between tube and column; Tube segment connections). The specifics of the model are described below with the theory of the elements shown in Section 2.2.

**Rail**
Both the rail and tube are modelled with Euler-Bernoulli beams. The rail is modelled as a continuous beam while the tube is divided into segments with a spring in between to represent the welded section. The rail segments are also welded together in reality. However, the influence of the rail segment connections is assumed insignificant to the tube segment connections and therefore not included in the research. The rail is supported periodically by the tube with the assumption that the supports have infinite stiffness, resulting in monolithic connections. The connections assume the same displacements and rotations for both the rail and tube.

**Tube**
The hollow tube could be best modelled by shell structures due to the presence of a lot of interactive stresses in all directions. This research is focused on 1-dimensional elements, therefore the tube is modelled with Euler-Bernoulli beams connected with 2 spring-dashpot systems in between the segments: one for vertical stiffness and damping and one for rotational stiffness and damping.

**Columns**
The columns are built below the intersection of two tube segments to reduce the stresses on the welded section. The columns are modelled as spring-dashpot systems. The stiffnesses are significantly higher than the other used spring-dashpot systems. On top of the column, two spring-dashpot systems are modelled to represent the bearing between the tube segments and the column. Below, the columns are pinned by setting the vertical displacement to zero. In reality, the soil has some influence on the structure. More about the soil influence can be found in Section 6.

**Moving load**
The structure is loaded by a constant moving load acting along the rail, meaning the magnitude of the force is constant. In addition, the velocity of the load is constant, implying zero acceleration. The constant moving load lacks variation in time and has no coupling between the load and the structure. Therefore only resonance and dynamic amplifications can be observed due to the load's characteristic [29]. The dynamic amplification is a natural consequence of the interaction between the load and the system's properties, such as stiffness and damping, leading to resonance at certain frequencies.

## 3.2 FEM Description

The processes and methods used in the FEM model can be broken down and isolated visually in a flowchart. The flowchart is shown in Figure 3.2, representing the FEM model schematically. The chart provides a structural overview of the used methods to follow and understand the steps taken in the FEM model and can be seen as a visual roadmap. The rounded blocks mark the start and end of the chart. Arrows lead the path to the end, leading through various types of blocks with each their specific action. Straight rectangles represent the processes in the FEM model, parallelograms represent the output of the processes and the diamond squares indicate a decision.

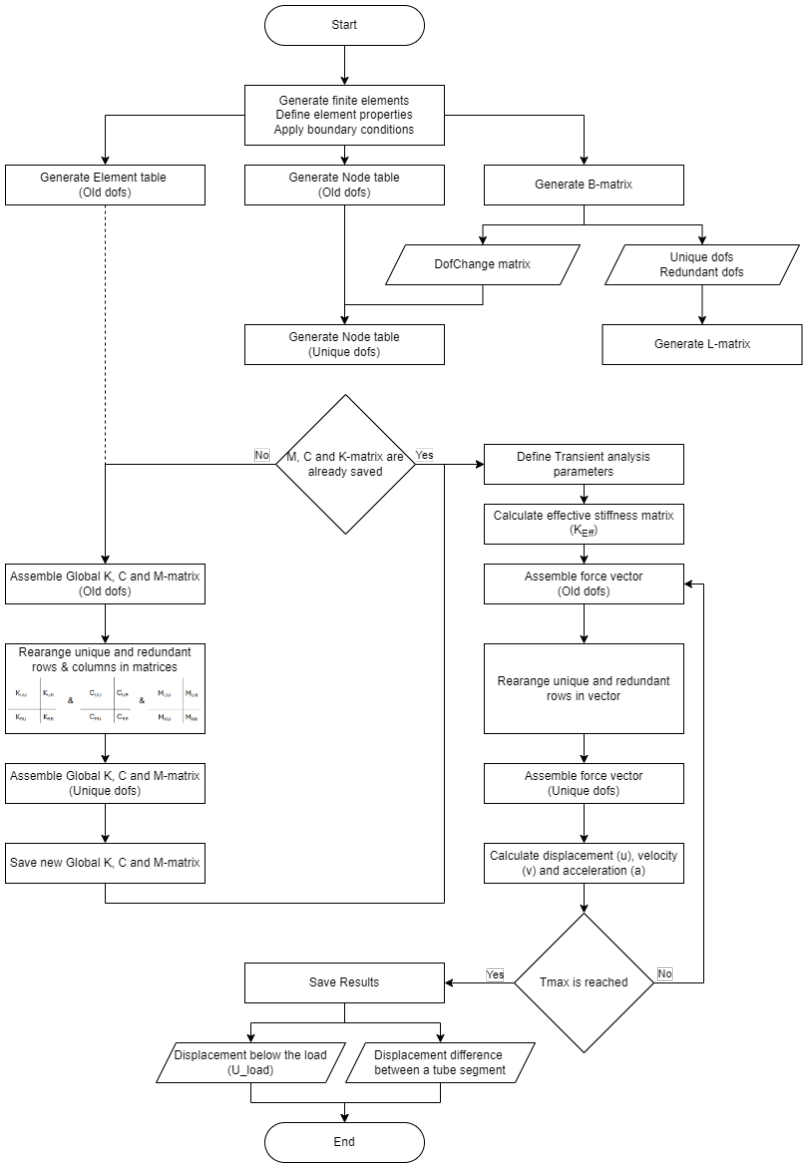


Figure 3.2: Flowchart of the Finite-Element Model

Initially, the model defines the elements with their properties within the domain. The boundary conditions at the ends are defined and proved insignificant due to the use of the absorbing boundary layers. Despite the minimal influence, the Dirichlet boundary conditions set the displacement at the end nodes to zero ($\mathbf{u} = 0$) and the Neumann boundary conditions set the rotation at the end nodes to zero ($u' = \theta = 0$). The model is constructed in cells, shown in Section 3.1, resulting in degrees of freedom (dofs) that must be merged. The connections between the rail and tube have to be merged as well to describe the same displacement and rotation. Therefore, the Boolean matrix (B-matrix) is generated. The matrix enforces the compatibility condition of the interface dofs [30]. The interface dofs will be merged and must satisfy the compatibility condition; both dofs need the same displacements or rotations ($\mathbf{Bu} = 0$) The Boolean matrix can be used to determine the unique and redundant dofs. The redundant dofs will be merged into other dofs in the new system to remain with the unique dofs. The new system has fewer dofs and a matrix (DofsChange matrix) is built to update the Node table with the new node numbers based on the unique dofs only.

The Boolean localization matrix (L-matrix) is based on the derived unique and redundant dofs and plays a critical role in coupling the dofs to serve as a bridge between the reduced set of unique dofs ($\mathbf{q}$) and the full set of interface dofs for the system ($\mathbf{u}$). The L-matrix is constructed in such a way that the compatibility condition is automatically satisfied and can be expressed in terms of the unique dofs as well ($\mathbf{BLq} = 0$). Each row of the L-matrix corresponds to one of the unique degrees of freedom, while each column corresponds to a degree of freedom in the full system. Besides the compatibility condition, the force equilibrium condition has to be met to ensure no unbalanced force or instability. The condition is met when the sum of all forces at an interface is zero. The transpose of the L-matrix ($\mathbf{L}^T$) and a vector of the forces ($\mathbf{g}$) are used for the mathematical representation ($\mathbf{L}^T\mathbf{g} = 0$).

Before assembling the mass matrix ($\mathbf{M}$), the damping matrix ($\mathbf{C}$) and the stiffness matrix ($\mathbf{K}$), a check is performed to determine whether the matrices are already stored on the local computer drive. The matrices are stored after each assembly to save calculation time. The matrix assembling is time-consuming, especially in the non-moving reference frame due to the need for a larger domain. The check is done by comparing the input values of the calculation and the saved matrices. If all relevant values match, the stored matrices are used and the FEM model goes directly to the transient analysis. If not, the matrices are built with the weighted residual method using the Galerkin method, which is shown in Section 2.3. The local matrices describe the behaviour of an element. To describe the whole domain correctly, all local matrices have to be added to the global mass, damping and stiffness matrices. The positions of the local matrices in the global matrices are based on the dof-numbers assigned before. When all elements are included, the global matrices describe the whole domain including the redundant dofs. During the assembling, sparse matrices are used. This type reduces the number of stored elements by excluding elements with zero values. Resulting in an efficient storage, especially if most of the elements of the matrix are zero. The built matrices are rearranged with first the unique dofs followed by the redundant dofs. The translation is executed with the generated L-matrix to obtain the matrices of the new dofs system, shown in Equation 3.1. The matrices are saved on the local computer drive with their input values to use in another

$$\tilde{\mathbf{M}}\ddot{\mathbf{q}} + \tilde{\mathbf{C}}\dot{\mathbf{q}} + \tilde{\mathbf{K}}\mathbf{q} = \tilde{\mathbf{f}}, \quad \begin{cases} \tilde{\mathbf{M}} \triangleq \mathbf{L}^T\mathbf{M}\mathbf{L} \\ \tilde{\mathbf{C}} \triangleq \mathbf{L}^T\mathbf{C}\mathbf{L} \\ \tilde{\mathbf{K}} \triangleq \mathbf{L}^T\mathbf{K}\mathbf{L} \\ \tilde{\mathbf{f}} \triangleq \mathbf{L}^T\mathbf{f} \end{cases} \tag{3.1}$$

After building the mass, damping and stiffness matrix, only the force vector is missing. The vector is made in the transient analysis due to its time dependence. If the moving load has a velocity, the force acts each time step at a different location on the rail. Resulting in a different force vector at each time. Before the transient analysis, the transient parameters are defined including the gamma and beta values of the Newmark method. $\gamma$ and $\beta$ are respectively $\frac{1}{4}$ and $\frac{1}{2}$ to ensure unconditionally stability as explained in Section 2.4. In addition, the effective stiffness matrix ($\mathbf{K_{eff}}$) is calculated before the analysis due to the time independence of the matrix. In the transient analysis, the force vector is built at each time step for the full dofs system and translated to the unique dofs system with Equation 3.1. After the transition, the Newmark method can be applied to the new system. The method is described in more detail in Section 2.4 and gives the displacement, velocity and acceleration for each unique node at each time step. The parameters are used to find answers to the research questions by means of the parametric study in Section 5.

## 3.3 Model Validation

The model is developed progressively. At each developed phase, the model undergoes intensive testing and validation to ensure the simulations' accuracy and reliability. From validating an Euler-Bernoulli beam on a Winkler-foundation to an Euler-Bernoulli beam periodically supported with a given stiffness. The last validation is done with an analytical model created in MatLab for different velocities of the moving load [31]. The parameters are tweaked to the validation data. The results of Matlab are transformed to Python and compared to the model with an Euler-Bernoulli beam periodically supported by springs for different velocities. All investigated velocities had the same phenomena difference. Therefore, only the results of one velocity ($V = 100m/s$) are shown in the report.

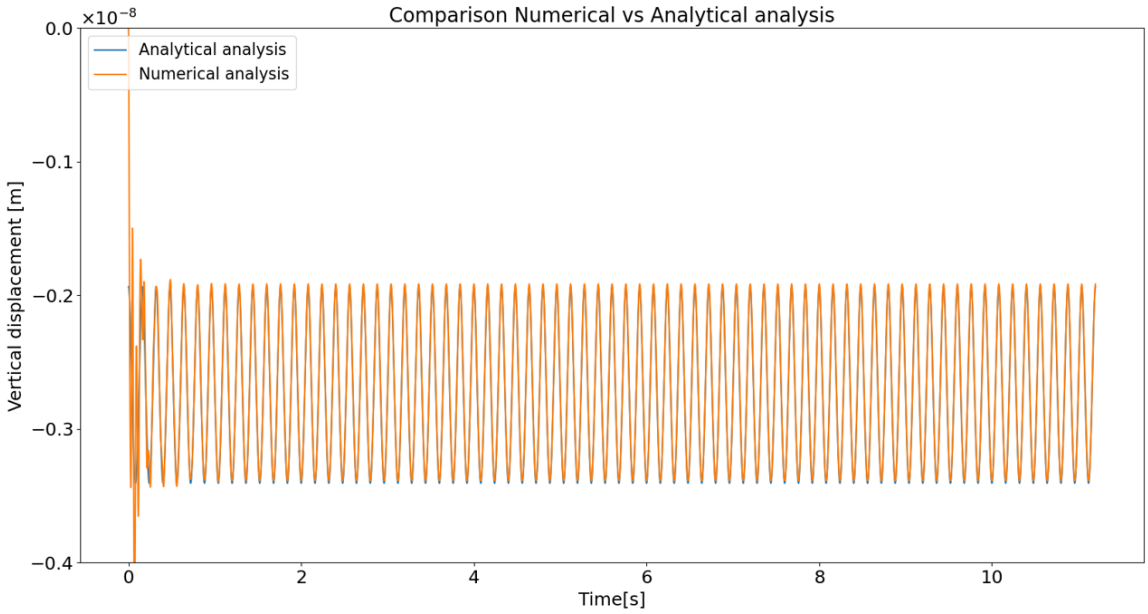


Figure 3.3: Comparison numerical vs analytical analysis

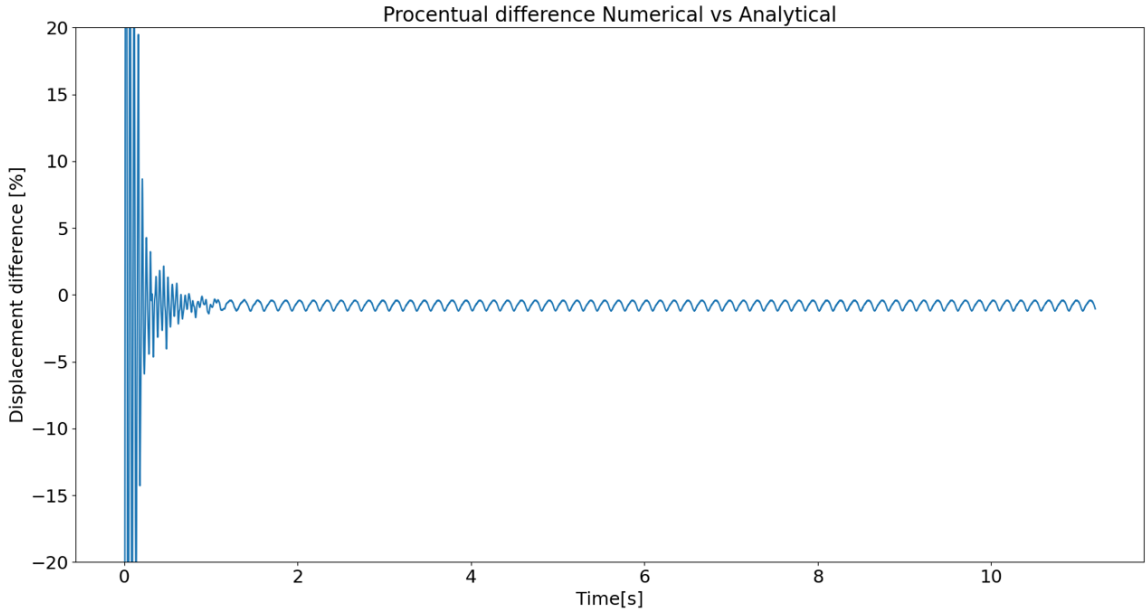


Figure 3.4: Procentual difference numerical vs analytical analysis

All investigated velocities had the same differences in phenomena. Therefore, only the results of one velocity ($V = 100m/s$) are shown in the report. Figure 3.3 shows the vertical displacement below the moving load for both the test model (numerical analysis) and the validation model (analytical model). Figure 3.4 shows the percentage difference between both analyses:

$$u_{\text{diff}}\,[\%] = 100 \times \frac{u_{\text{numerical}} - u_{\text{analytical}}}{u_{\text{analytical}}} \tag{3.2}$$

The difference between both models can be found at the start of the analyses. The numerical model requires an initial incubation period before reaching stable and meaningful results in contrast to the analytical model. The incubation phase is also known as the transient phase and occurs due to the iterative nature of numerical simulations where the model needs to adjust to the imposed boundary and initial conditions [32]. In the analytical analysis, the results are derived directly from mathematical expression and are focussed on the steady-state response. After the transient phase, the difference between both analyses is insignificant due to the different implementation of the domain boundaries. The validation model connects the last cell with the first cell again, while the numerical model makes use of an absorbing layer to damp out the propagating waves at the boundaries.

## 3.4 Numerical Stability

After the validation, the model is expanded to the model shown in Figure 3.1. An extra beam and several springs are added. The additional element could cause instability. The type of instability is described in Section 2.6. The instability is prevented by conducting many runs with varying input parameters. The time step and element size parameters get a thorough analysis due to their importance in the model stability. Both parameters have the same trade-off, model accuracy versus computation time. The challenge lies in identifying the lowest computation time with acceptable accuracy. The approach is working top-down, meaning the process starts with a large element size and time step. The parameters will be gradually reduced one at a time until the results meet acceptable accuracy standards. Resulting in a limit for both parameters. The span of the rail support is governing for the largest element size. The model is constructed in cells, which are put in sequence. Each cell has the first rail support at half the rail span distance from the boundary. With a standard span of one meter, the element size must be half a meter or less. For the time step size, the velocity and Column span are key factors. For low speed, an oscillating curve is expected for the vertical displacement under the load, one oscillation per column span to be exact. If during one time step a whole column span is skipped, aliasing occurs and information is lost in the calculation. The representation of one oscillation needs at least 10 data points [33]. After testing, the amount of steps is set to fifty per column span. Resulting in the time step size limit shown below:

$$Element\,size \leq 0.5\,\text{m} \quad ; \quad \Delta t = \frac{1}{50}\frac{Column\,span}{Velocity\,moving\,load} \tag{3.3}$$

## 3.5 Damping

A damping analysis is executed to ensure valid outcomes since the displacement went to zero when the influence of the column stiffnesses was tested over the operational velocities. This phenomenon indicates too much damping in the model according to a MatLab script describing a periodic supported Euler-Bernoulli beam [34]. If the displacement goes to zero without a peak, the dynamic amplification is not captured and the damping has to be decreased. The damping is only added to the model to stabilise and give a realistic response. The damping ensures the model has an energy outlet and captures the effect of friction and energy losses caused by other mechanisms.

The damping is investigated by setting the damping proportional to the stiffnesses of the model elements. First, the same proportions were used for both the beam and spring damping, resulting in a governing beam damping due to the significantly greater stiffness magnitude. Therefore, the damping of the tube and rail are set fixed ($CEI_{\text{Tube}}$=0.001 Ns/m and $CEI_{\text{Rail}}$=0.00001 Ns/m) and the spring damping is proportional to their stiffnesses. Figure 3.5 gives an insight into the behaviour of the displacement for different damping values over the velocity. The small fluctuations in the lines can be caused by the chosen mesh size. The element size is set to 0.5 meters, resulting in only two elements between the consecutive rail supports. The element size can be reduced to reduce the small fluctuations consequently increasing the computation time. The other option is to model the periodic supports as a continuous foundation since the pod can travel across up to 300 periodic

supports per second based on the upper limit of the operational velocity range. The small fluctuations were addressed in a later stadium, resulting in the use of periodic supports and the element size set to 0.5 meters with a recommendation to use a continuously supported rail in future research.

The peak in the figure indicates the point where the tube experiences a significantly larger displacement. The dynamic amplification occurs due to resonance effects. At the peak, the velocity of the constant moving load approaches a critical velocity of the structure and the frequency of the applied load matches a natural frequency of the modelled system. The system could have infinite natural frequencies. The model operates in the time domain with velocities up to 300 m/s. Within the operational velocity range, only one peak is obtained as can be seen in Figure 3.5. The peak can be indicated by the main critical velocity due to the most occurring resonance. The different damping levels affect the sharpness and magnitude of the dynamic amplification peak. The higher the damping, the smoother the displacement range change. If the damping is too high, the model loses information and cannot capture the peak at the velocity of 230 m/s of the moving load. Therefore the damping of the springs (dashpots) in the model must give a smooth line without losing significant information about the system. Therefore is the damping set to 0.1% of the spring's stiffnesses. The damping could have been set even lower by improving the mesh size, resulting in a trade-off with the computation time. In addition, the conclusion can be made that the damping does not have an influence on the value of the main critical velocity since the peak stays at the same velocity independent of the damping value.

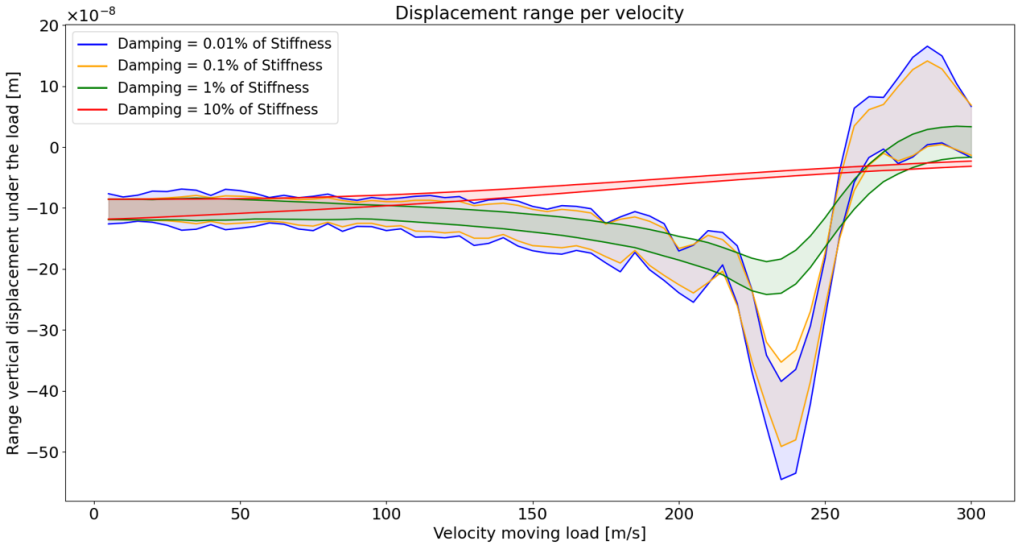


Figure 3.5: Displacement range of periodic cycle for different damping values

# 4 | Moving Reference Frame Model

The moving reference frame model considers the load as stationary while the structure moving beneath, in contrast to the non-moving reference frame, where the structure is fixed and the load moves across. The principles of a moving reference frame can be an outcome to reduce the domain size, hence the computation time [35]. Especially for the Hyperloop concept, since the Hyperloop pod has operational velocities of up to 300 m/s. The focus lies on the dynamic response around the moving pod. With a non-moving reference frame, the domain must already have a length of at least 1500 meters for a simulation of five seconds. The domain of the moving reference frame must only be sufficiently large to damp out the propagating waves moving away from the load, resulting in no relation between the domain size and the simulation time. Therefore, a moving reference frame is preferable for the modelling of a Hyperloop system.

The moving reference frame is unconventional within the research field. In this chapter, the moving reference frame is investigated for a continuous and periodic supported model. The two models are simplistic to ensure stability within the finite element models. The models are explained below, whereupon the processes and methods used in the finite element model are discussed and concluded by a validation of the models.

## 4.1 Model Description

Both model representations have an Euler-Bernoulli beam with a constant load on top, representing the pod's force on the Hyperloop tube. The location of the load is fixed in the centre of the domain with the beam sliding beneath the load over time. The difference between the models is the type of foundation. The first model is shown in Figure 4.1 and is continuously supported with a Winkler foundation. The second model supports the beam periodically with springs acting as columns and is shown in Figure 4.2 Both models execute a steady-state analysis and a transient analysis. The steady-state analysis for the periodic supported beam is not time-independent due to its time-dependent boundaries. Therefore a periodic steady-state is considered.

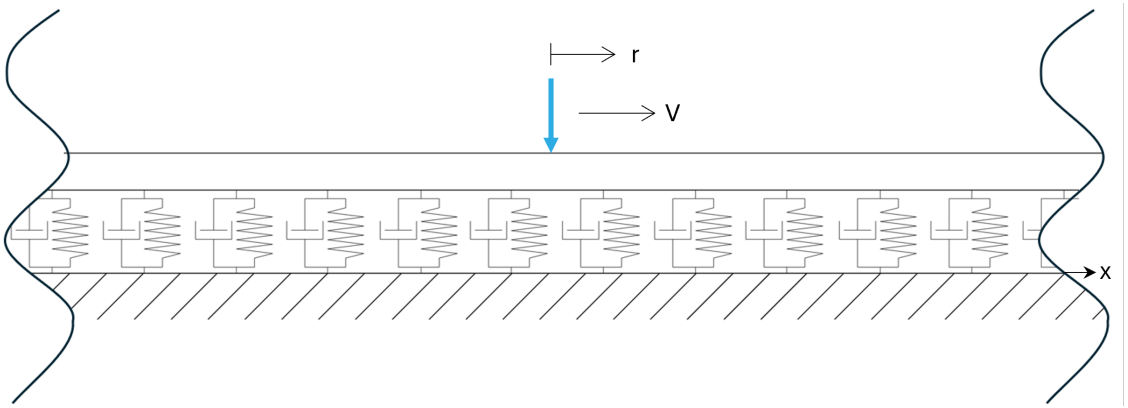


Figure 4.1: Schematic representation of continuously supported beam

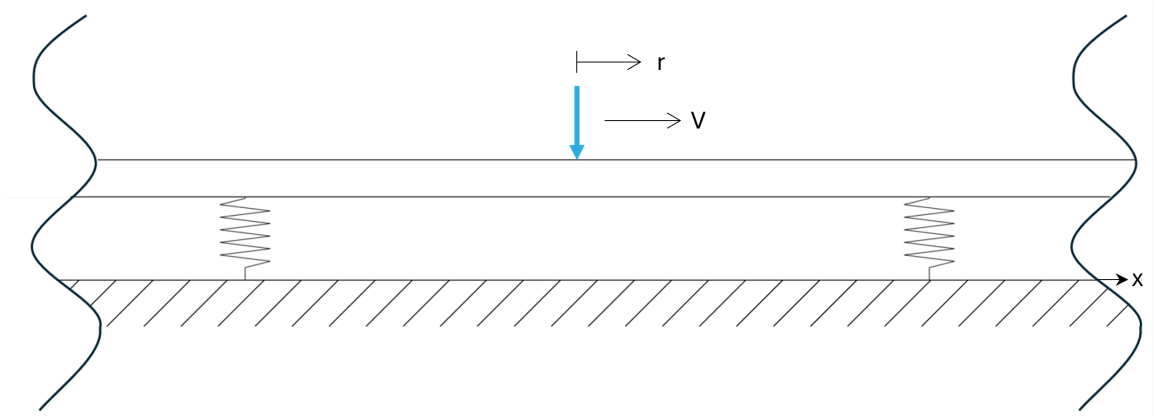


Figure 4.2: Schematic representation of the moving reference frame model

The models are described by different equations of motion. First, the equations of motion for a non-moving coordinates system are described to transform the equations easily to the moving coordinates system. The continuously supported beam is shown in Figure 4.1 with an elaboration in Section 2.2. The periodic supported beam has a slightly different equation of motion, since the equation includes a Dirac delta function to represent the periodicity in the model. Figure 2.1 shows the equation of motion still in the non-moving coordinates system.

$$m\ddot{u} + EIu'''' + c\dot{u} + ku = f \tag{4.1}$$

$$m\ddot{u} + EIu'''' + c\dot{u} + ku + k_p \sum_n \delta(x - x_n)u(x,t) = f \tag{4.2}$$

The key consideration for the moving reference frame is the coordinate transformation. The coordinates system is changed from the global non-moving coordinates ($x$) to the moving reference system ($r$) with the load fixed with Equation 4.3. The global coordinates are only space-dependent, while the moving reference system is both space and time-dependent.

$$x = r + Vt \tag{4.3}$$

The equations of motion for the moving reference frame are based on the coordinate transformation. Equation 4.3 can be substituted into Equation 4.1 and 4.2 to write the equations in the moving reference frame.

$$EIu'''' + m\left(V^2u'' - 2V\dot{u}' + \ddot{u}\right) + c(r)\left(\dot{u} - Vu'\right) + ku = F_r\delta(r) \tag{4.4}$$

$$EIu'''' + m\left(V^2u'' - 2V\dot{u}' + \ddot{u}\right) + c(r)\left(\dot{u} - Vu'\right) + k_{spring}\sum_n \delta(r + Vt - x_n)u(r,t) = F_r\delta(r) \tag{4.5}$$

The only difference between the equations is the stiffness term and the implementation of the damping term. The distributed damping ($c(r)$) is included in both models to use for the absorbing boundary layers as explained in Section 2.5. In Equation 2.21, a constant distributed damping is present within the boundary layers ($c > 0$) for the model with the continuously supported beam. Additionally, a constant distributed stiffness is present to represent a Winkler foundation correctly. For the periodically supported the constant distributed damping is set to zero ($c = 0$). Here, the damping is generated only by the dashpots and tube and the stiffness is generated by the springs and bending stiffness of the tube.

## 4.2 FEM Description

The processes and methods of the steady-state analysis and the transient analysis used in the moving reference frame models are depicted in a similar flowchart format as in Section 3.2, providing a schematic representation of the modelling approaches. The flowcharts in Figure 4.3 display the key steps involved in both analyses for both described models. The charts are more straightforward due to no change in the coordinate system within the model. The coordinate system is already changed in the equation of motion. In addition, only one Euler-Bernoulli beam with two different types of supports is considered in comparison with the complex model shown in Figure 3.1.

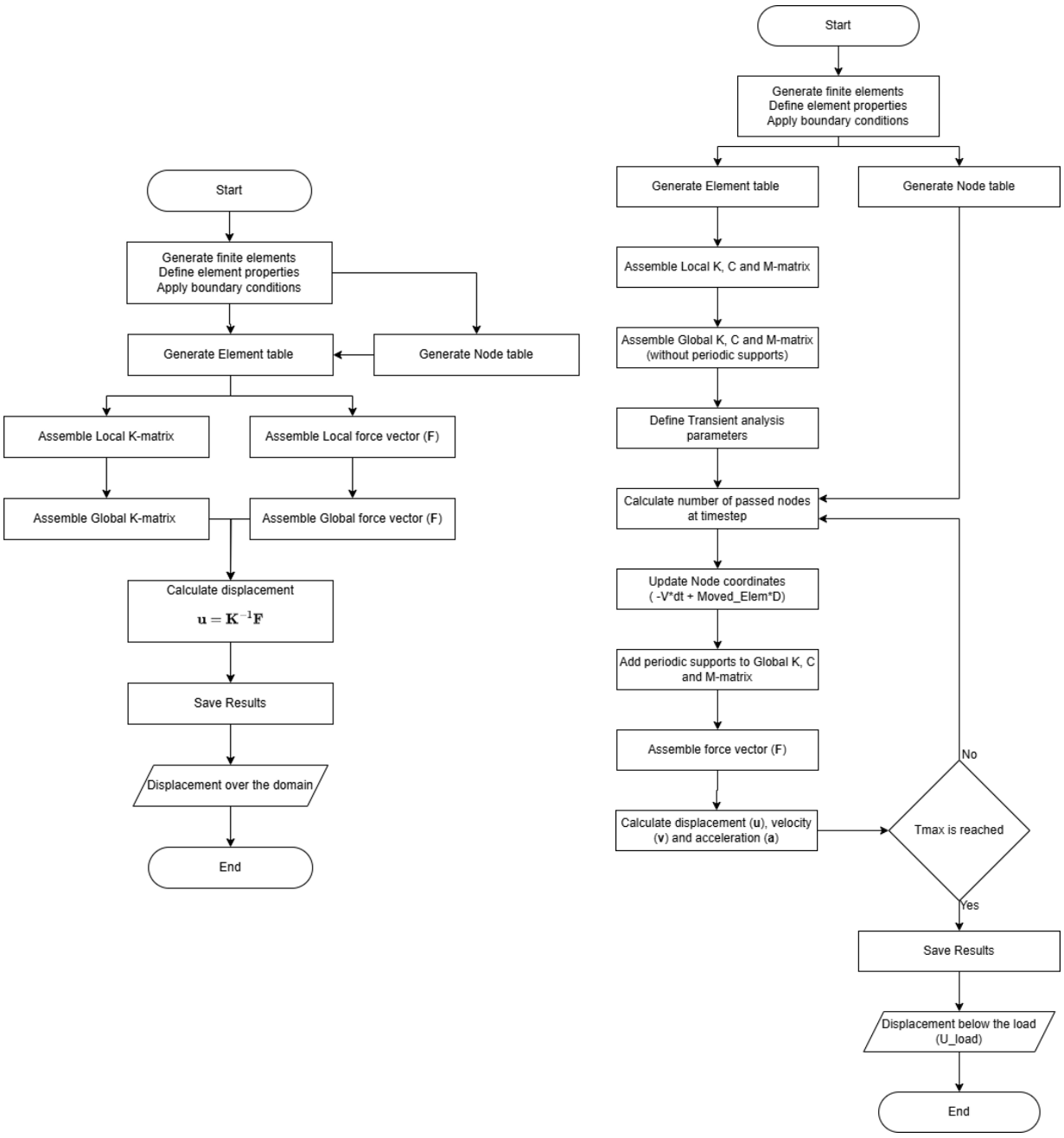


(a) Steady-State analysis (b) Transient analysis

Figure 4.3: Flowcharts in the moving reference frame

The models have many similar processes and methods. Nevertheless, the models will be treated separately. First the general methods, used for both analyses, are elaborated. After, the specifics of the steady-state model are shown, followed by the specifics of the transient analysis.

The model starts as each FEM model, by defining the domain with their properties. The node table and element table can be derived from the defined domain with its properties. The node table contains all nodes with their coordinates which are included in the element table. In addition, the table contains the element types and their properties of all elements. The tables are used to derive the global matrix of the equation of motion. After successfully building the model in the moving reference frame, the same Galerkin method was applied as in Section 3.

In contrast with the non moving reference frame model, the system matrix is not symmetric due to the presence of the velocity of load in the matrix. Therefore, the least squares method is used to overcome the instability compared to the Galerkin method. The advantage of the least squares method is the created symmetric system of algebraic equations. The system matrix is in addition also positive definite, since the diagonal entries are always positive [36]. The basic idea behind the residual computation of the least squares method can be found in Section 2.3. The calculated matrices are embedded within a Python function, where the model parameters are represented symbolically to enhance flexibility and adaptability. This approach allows the finite element model to invoke the function and substitute the relevant parameters into the matrices. The substitution of the parameters is done in separate functions isolating the matrices. This setup ensures that the models remain resilient to variations in these parameters, facilitating efficient recalculation and analysis under different loading and material conditions.

Now the local system matrices are integrated into the model, the assembly of the global matrices can start by adding the local matrices into the appropriate positions within the global matrix, according to the degrees of freedom associated with the described elements. In the model with a continuous support, all elements can be described by the local matrices, facilitating the properties of the overall system. For the periodically supported beam, the supports must still be included by adding the support stiffness and damping to the global matrix.

**Steady-state analysis**
In the steady-state analysis, the support stiffness and damping are added directly afterwards due to no time dependence. The time dependence is excluded from a steady-state analysis by removing all time-dependent terms out of the equation of motions, stated in Equation 4.4 and 4.5. Therefore, the analysis is significantly faster since the displacements of the whole domain can be calculated directly when the global K-matrix and global F-vector are known.

**Transient analysis**
The transient analysis calculates the displacement of the whole domain per time step. Before the transient analysis can be executed, the parameters for the transient analysis must be specified. The parameters provide details regarding the constant moving load, the duration of the analysis and the time-stepping interval ($\Delta t$), ensuring that the simulation captures the system's dynamic response accurately per time step. In contrast to the non-moving reference frame model, the stiffness and damping of the periodic supports are included in the transient analysis in the moving reference frame model due to the time dependency. The supports change position at each time step, resulting in different positions of the degrees of freedom in the global system matrices. By attaching the supports each time step to the global matrices, the varying positions of the supports are accurately included throughout the simulation, capturing their impact on the system's transient response. The three matrices are merged into one matrix, called the effective stiffness matrix ($K_{eff}$). The force vector is created in the same way as in the non-moving reference model. Also, the same Newmark parameters are used to ensure unconditional stability. The Newmark method is described in Section 2.4 and gives the displacement ($u$), velocity ($v$) and acceleration ($a$) at each node at each time step.

## 4.3 Model Validation

This section outlines the development of the model along with the validation. The validation is necessary to answer the research question related to the possibility of modelling the system in the moving reference frame. Four calculations are considered: both models are validated for both the steady-state analysis and the transient analysis. The validation process is essential in guiding the model's development and improving its robustness, especially in the presence of stability challenges. Additionally, The model validation helps identify and address the potential instability issues that may occur. The model began by establishing correctness for simpler cases before introducing complex factors. In some cases, extra features are added to the tested model to order to compare the available literature. For instance, a distributed load is added to validate the Steady-State model to Seong-Min Kim's paper [37].

### 4.3.1 Steady-State Model with Distributed Foundation

The first validation is done for an Euler-Bernoulli beam resting on a distributed foundation in the moving reference frame. This approach ensured that the basic components of the model behaved as expected before incorporating additional complexities. Basu's analytical solutions for the Euler–Bernoulli beam on a visco-elastic foundation subjected to moving load are benchmark results to execute the first validation [38]. The model parameters are aligned with those from the validation dataset. Basu utilises $\alpha$ and $\beta$ respectively for the critical velocity and the critical damping. The critical velocity is the velocity at which the first waves propagate away from the load. The critical damping occurs when the system returns to equilibrium without oscillating. The critical values are case-specific. In Equation 4.6, the critical values for an Euler-Bernoulli beam with a distributed spring-dashpot foundation are shown [39].

$$V_{cr} = \sqrt[4]{\frac{4kEI}{m^2}} \quad ; \quad c_{cr} = 2\sqrt{km} \tag{4.6}$$

Comparing Figure 4.4, 4.5 and 4.6, the tested model behave similarly to the validation model for the different alpha and beta values although the absolute values differ slightly. An explanation could be that the shear interaction between the springs in the foundation according to Vlasov and Leont'ev [40] result a smaller amplitude of the validation data, since the interaction is not included in the tested model. The shear could also have an influence on the frequency in front of the load when the speed is twice the critical velocity. Since the validation set does not match the tested model precisely, another validation dataset was also consulted.

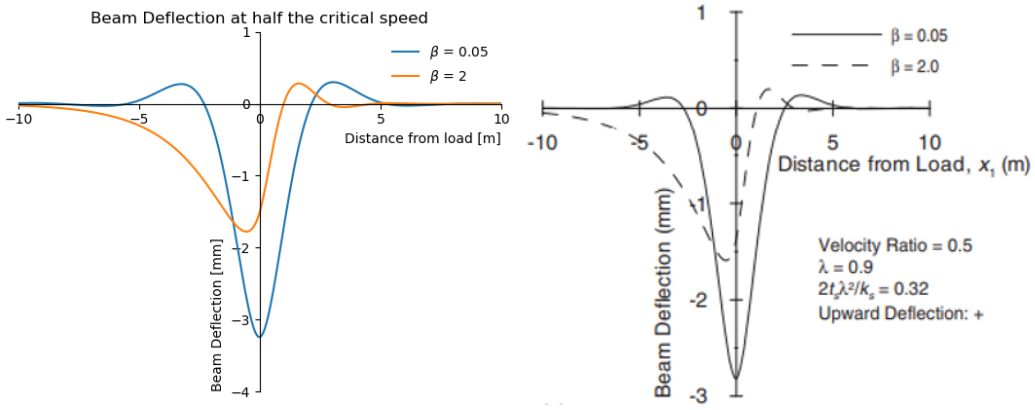


(a) Tested model's data (b) Validation data [38]

Figure 4.4: Validation comparison for $0.5V_{cr}$

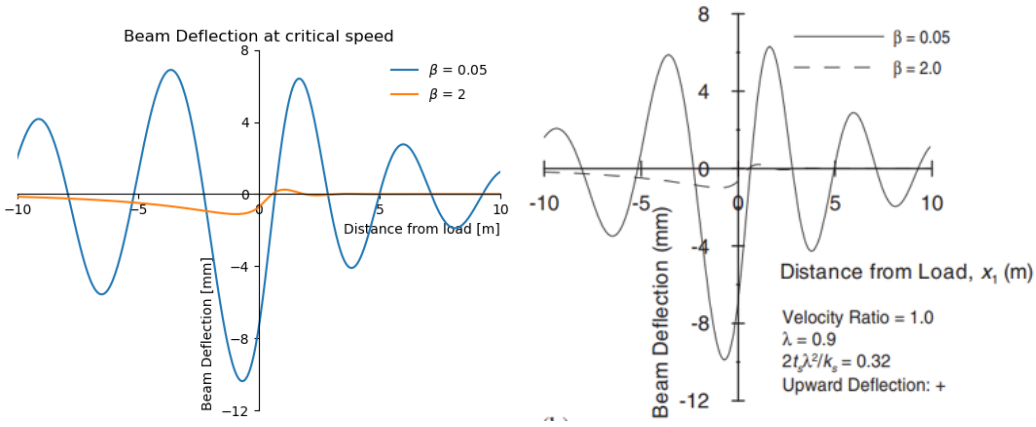


(a) Tested model's data (b) Validation data [38]

Figure 4.5: Validation comparison for $V_{cr}$

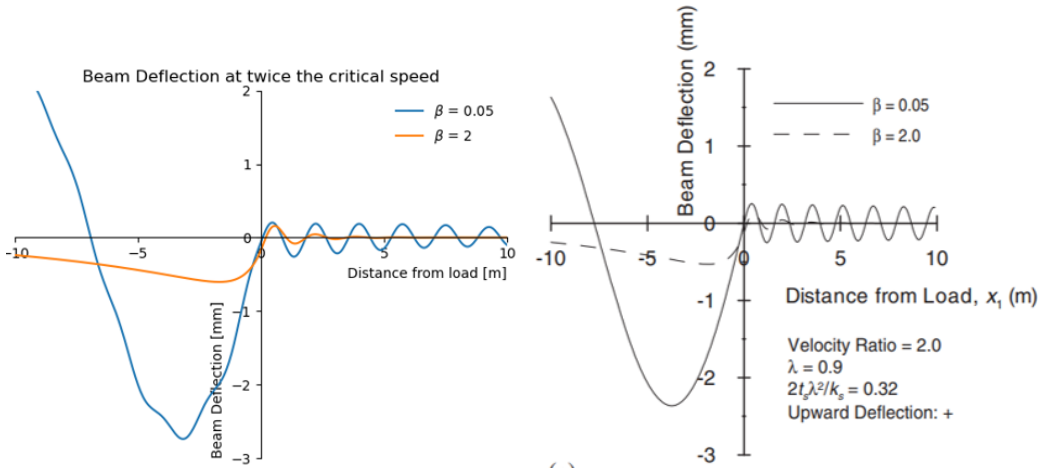


(a) Validation at $2V_{cr}$ (b) Validation data [38]

Figure 4.6: Validation comparison for $2V_{cr}$

Kim's model does not have shear interaction and makes use of a short distributed force[37]. The distributed force feature is built into the model and gives the beam deflection for velocities used in the validation dataset. Both Figure 4.7a and 4.7b show the result of the system without damping. Comparing both datasets shows that the validation was successful. Per velocity, the beam deflection shape around the load is the same with the amplitude having the same order of magnitude.

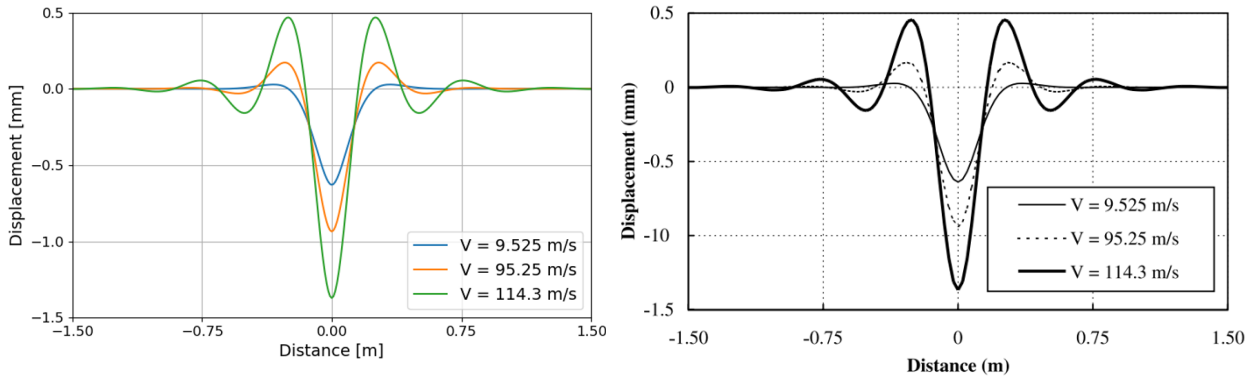


(a) Tested model's data (b) Validation data

Figure 4.7: Beam deflection for different velocities

### 4.3.2 Transient Model with Distributed Foundation

The subsequent step is adding a transient analysis to capture time-dependent behaviour. The model is based on the derived steady-state model. First, the least squares method was applied according to Raut's procedure [41], which makes use of scaling factors. The factors are included to take into account the different physical dimensions between the equations in the residual. The different dimensions are a result of the use of the mixed formulation. Since no stable results were obtained due to assumptions and incomplete explanations in Raut's method, Rasmussen's thesis [24] was used to achieve stable results for the transient analysis. However, this approach also produced unstable outcomes. In Section 4.3.4, several potential factors are which could be investigated to address the instability.

### 4.3.3 Steady-State Model with Periodic Supports

Following the successful validation of the steady-state analysis of the beam on a distributed foundation, an attempt is made to replace the distributed foundation with periodic supports beneath the Euler-Bernoulli beam. Due to the nature of the periodic supports, the vertical displacement directly below the moving load is not expected to remain constant over time due to the time-dependent boundaries. However, the displacement is expected to repeat itself in a regular pattern. The predictable repetition qualifies as a form of steady state known as a periodic steady state, where the system's dynamic response is consistent periodicity rather than a constant value. The periodic steady-state analysis allows for the characterization of the displacement at specific locations relative to the supports. The periodic steady-state can be executed with numerous methods, both in frequency and time-domain [42]. Since no validation data for this specific configuration could be found in the existing literature, the analysis is not executed.

### 4.3.4 Transient Model with Periodic Supports

The analysis uses the same methods as for the model with a distributed foundation. Also, the instability in this analysis could not be overcome, despite extensive efforts. Typically, numerical instabilities arise due to poor mesh quality or time-stepping algorithms. Therefore, numerous simulations were conducted, varying the element sizes and time steps. However, these adjustments failed to improve the stability. Additional parameters were also incorporated into the stability analysis, yet no significant improvements were made. No causation between the parameter settings and the instability could be found and therefore expected not to be the critical factor.

The periodic supports are added to the global matrix after the matrix is assembled with the least squares method. To exclude the time when the periodic supports are added is the critical factor, the periodic supports can be added to the equation of motion directly by a Dirac delta function, similar to a semi-analytical model. However, this introduces the disadvantage of the semi-analytical model without proving its benefits. Therefore, the periodic supports are not included in the equation of motion. The factor can also be tested by assuming infinite column stiffness, resulting in no beam displacement at the support locations. The nodes at these locations are predescribed and excluded from the calculation, as only the free nodes of the global matrix are considered in the inverse of the matrix. The adaption in the model did not lead to stability in the analysis.

The last examined factor is the effect of the moving pod in the model by setting the velocity of the constant load to zero. With no moving loads, the instability remained. Even if the velocity of the pod was removed from the model, achieving stability remained elusive.

None of the examined factors were the critical factor causing the instability. Due to the limited timeframe of the research, the instability in the moving reference frame model could not be researched in further detail. Future research should focus on investigating the order of discretisation as a potential critical factor. The time discretisation before executing the spatial discretisation [43]. Herein, the least squares method stays the recommended spatial discretisation method since the method improves stability without compromising the accuracy. [36]. The first discretisation should focus on the most critical discretisation. The discretisation of the time domain addresses the rapid changes in the transient analysis caused by the pod travelling at velocities of up to 300 m/s, while the structure's geometry is modelled simply. The geometry does not match the complexity of the dynamic response, emphasizing the importance of prioritizing time discretization. Despite no stable transient analysis in the moving reference frame, the model validation has been essential in giving a better insight into the correctness of the model and the potential sources of numerical errors.

# 5 | Parametric Study

The parametric study investigates the influence and sensitivity of the parameters in the non-moving reference frame model, as the instability issues in the moving reference frame model could not be resolved within the available research time. In this parametric study, two types of analysis are executed on the model in Figure 3.1 to find the influence of different parameters on the structure's behaviour:

- The vertical displacement below the load is compared to different values of a specific parameter to find a correlation. The analysis is executed for several velocities.
- The vertical displacement difference between two tube segments when the load is on top to see the influence of the specific parameters on the tube intersection.

The focus of the analyses lies on the influence of the stiffness parameters at different velocities of the Hyperloop pod. The stiffnesses are shown in Figure 5.1 with a snapshot of a part of the complete model and are systematically varied to identify critical behaviours, such as resonance and displacement variations, which could affect the comfort of the passengers and even the overall structural integrity. This study is essential for refining the design and ensuring the robustness of the model, especially for the operating velocities. In this section, only the relevant results are addressed. Appendix C contains all obtained results to get the whole picture of the study.

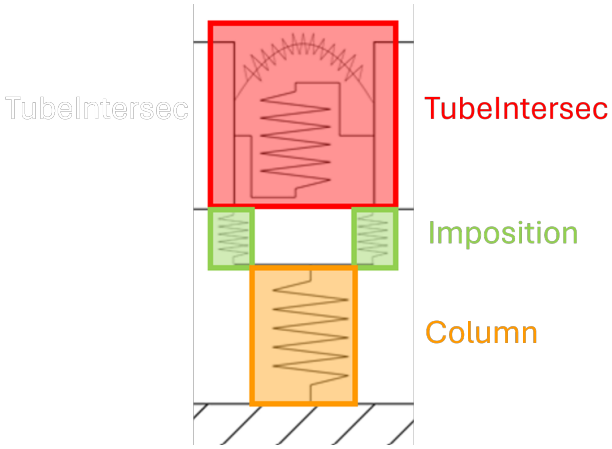


Figure 5.1: Spring description

All initial values in the analyses are based on Fărăgău's article [9] with a unit load of one acting on the rail downwards, resulting in no relevant absolute values. This study focuses on the relation between the different analysis values. The best approach is to use a non-dimensional parameter. This relative parameter gives a better insight into the behaviour of the structure in real life since reality corresponds with the relative value better. To match the absolute value, all parameters need to correspond exactly. For a periodic supported beam with discrete springs, the non-dimensional parameter $\alpha_v$ is found [44]. Since the investigated structure has more complexity, the relationships between different springs' stiffnesses and the tube's bending stiffness are not analysed with $\alpha$. Only the relation of the rail's bending stiffness with the tube's bending stiffness has been analysed with a non-dimensional parameter since both stiffnesses have the same dimension, resulting in the bending stiffnesses being divided by each other.

## 5.1 Vertical Displacement under the Moving Load

The vertical displacement under the moving load has a frequency due to the periodic supports. The displacement's frequency has a constant upper and lower limit. The analysis is executed for the three velocities 30 m/s, 100 m/s and 300 m/s, resulting in three different periodic frequencies of the vertical displacement under the moving load. Since the cycle has the length of the column span and the pod's velocity over the columns differs, the frequency has a linear relation and can be calculated by dividing the moving load velocity by the column span. In contrast to the damping, varying the stiffnesses have a significantly larger influence on the main critical velocity. Therefore, the three investigated pod velocities do not necessarily fall into the same wave propagation region for each analysis.

**Bending stiffness of the rail (Rail_EI)**
The correlation between the bending stiffness and the vertical displacement below the load is the same for the pod velocities of 30 m/s and 100 m/s. Figure 5.2 gives the influence of the different values of $\alpha$ on the vertical displacement under the moving load with a velocity of 30 m/s. The non-dimensional parameter is written as follows:

$$\alpha_{Rail} = \frac{EI_{Rail}}{EI_{Tube}} \tag{5.1}$$

Increasing the $\alpha$ gives a lower displacement and fluctuation. The displacement reduces linearly by increasing the non-dimensional parameter. The fluctuations of the higher alpha values are low but still present despite the unclear representation in the figure.

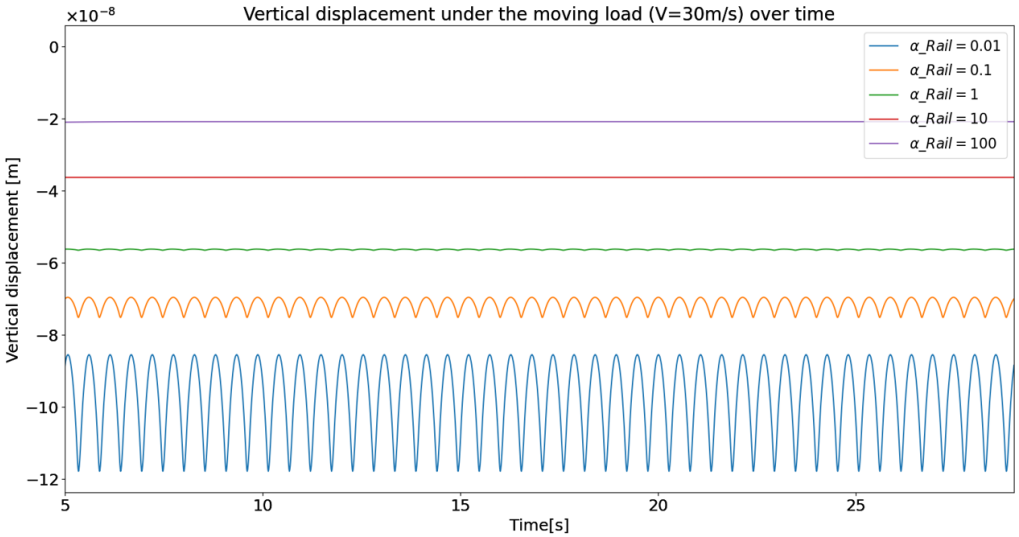


Figure 5.2: Vertical displacement with a moving load of 30 m/s for different bending stiffnesses of the rail

The altering of the rail's bending stiffness with a pod velocity of 300 m/s gives the results shown in Figure 5.3. The responses do align with the relation made before and have still the same phenomena for almost all bending stiffnesses of the rail, concluding that these sets of properties stay in the same wave propagation region with respect to the main critical velocity. One outlier is found and has a rail's bending stiffness of 1% of the initial tube's bending stiffness. Although the fluctuation of the outlier is still in the same order of magnitude, the outlier's displacement is significantly lower compared to the results of 30 m/s. Therefore the main critical velocity is exceeded for the specific set of properties if the pod velocity is 300 m/s and the other higher bending stiffnesses are all still below the main critical velocity. In addition, the rail's bending stiffness has a positive relation with the main critical velocity: the lower the rail's bending stiffness, the lower the main critical velocity within the operational velocity range. The relation is based on Figure 5.2 and 5.3 and confirms the already existing literature.

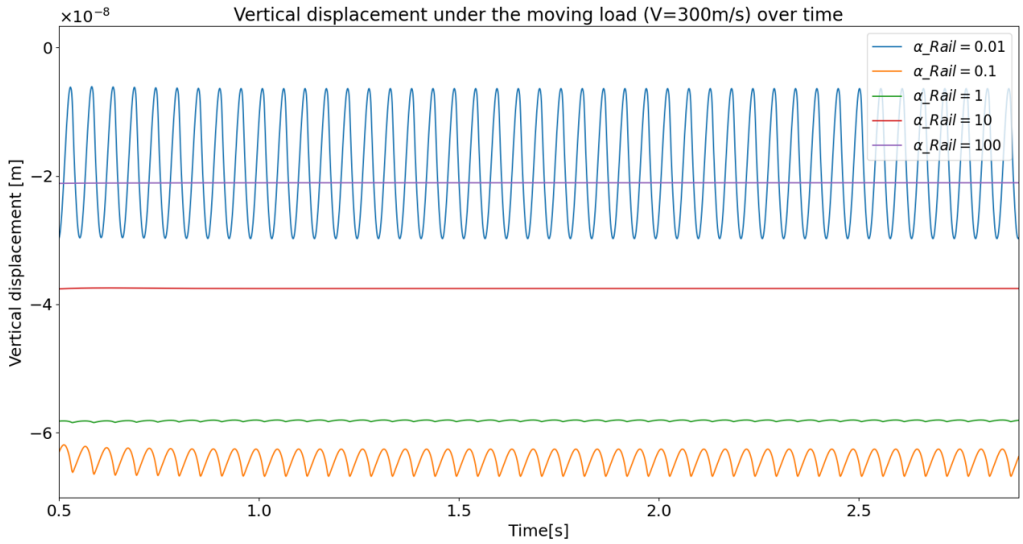


Figure 5.3: Vertical displacement with a moving load of 300 m/s for different bending stiffnesses of the rail

In the previous analysis, the initial value of the tube's bending stiffness is used as the benchmark value ($EI_{Tube}$) in the non-dimensional parameter ($\alpha$). This analysis is executed to find the influence of the stiffness' magnitude for the same $\alpha$'s. Therefore both bending stiffnesses are decreased by $\frac{1}{100}$ of the initial bending stiffness. Figure 5.4 shows the $\alpha$'s from 0.01 up to 100 with a reduced stiffness. The analysis gives the same relations as before at a velocity of 30 m/s: the higher $\alpha$, the lower the mean displacement and fluctuation. Despite the same relations, the displacement and fluctuation are more extreme due to the stiffness decrease of the total system. The non-dimensional value does not say anything about the total stiffness, only about the relation between the different stiffness values. The lowest stiffness represented in Figure 5.4 is $\alpha_{Rail}$ equal to 0.01 and has an unexpected kink at the top of the cycle. Also, the representation of $\alpha_{Rail} = 0.1$ has an asymmetry. So far, no explanation for these phenomena has been identified. An option is the wrong time step settings, which could have been tested by decreasing the time step size.

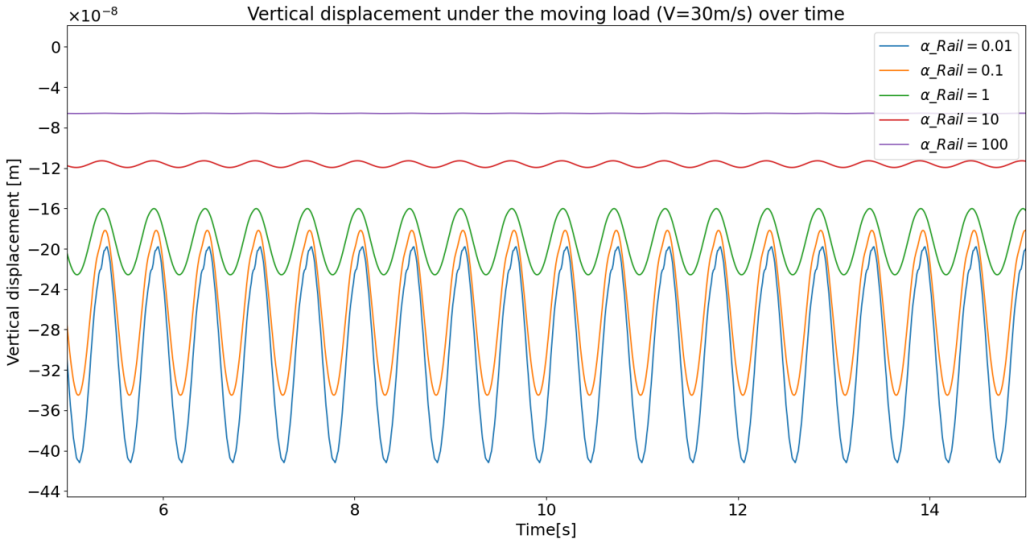


Figure 5.4: Vertical displacement with a moving load of 30 m/s for different bending stiffnesses of the rail with reduced values

**Vertical stiffness of the imposition spring (K_imposition)**
For the stiffness of the imposition spring, the mean displacement and fluctuation decrease by a higher stiffness as well. However, the displacement relation is not linear as for the rail's bending stiffness. The displacement runs to an asymptote by increasing the imposition stiffness. The imposition stiffness is increased by 10, resulting in a smaller displacement difference each time. As a result, the four highest stiffnesses align and no difference can be obtained in the figure. Therefore, the stiffness can be seen as infinite and the imposition spring stops influencing the system response due to the effect of other governing springs. The pits in the graph at the lowest point of the displacement cycle could been caused by transition radiation, despite its continuous presence. The radiation is emitted when a source without an inherent frequency moves rectilinearly with constant velocity and acts on or near an inhomogeneous medium [45], meaning a sudden stiffness increase can result in radiation, which is captured by the dip in the graph. Another explanation could be a not optimal finite element discretization.

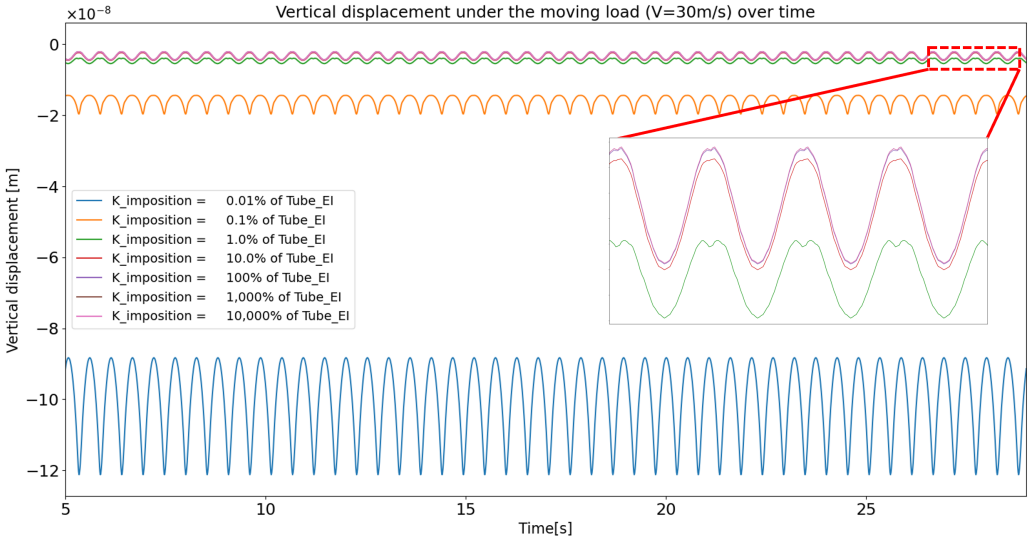


Figure 5.5: Vertical displacement with a moving load of 30 m/s for different stiffnesses of the imposition spring

In Figure 5.6, the displacement under load is plotted over time for a moving load of 300 m/s. Comparing the response to the load moving with 30 m/s, the plots have still the same phenomenon for the mean displacement running to an asymptote by increasing the stiffness with one outlier. The blue line represents the outlier and has a significantly lower mean displacement compared to the 30 m/s case. The outlier can be explained by the main critical velocity, which can be seen in Figure 3.5 for a random set of properties. The change in the set of properties, results in a change in the main critical velocity. For the blue line's specific set of properties, the main critical velocity of the structure is lower than 300 m/s, giving a lower mean displacement compared to velocities below the main critical velocity of the structure. So an increase in the stiffness of the imposition spring increases the main critical velocity of the system.

The imposition stiffness and the amplitude of the deviation have a negative correlation: the higher the stiffness, the lower the amplitude of the deviation. However, the green line breaks the correlation and is significantly less symmetric than the response of the other set of properties. The higher imposition stiffnesses have also a kink on the top of the cycle, which is observed before in Figure 5.4. The asymmetry of the green line looks like an exaggeration of the higher stiffnesses' kink at a different location of the cycle. The exact location relative to the locations of the supports cannot be obtained from the figures. For analyses involving a low velocity of the moving load, the support's location can be assumed with sufficient confidence to correspond to the lowest displacement in the cycle. In contrast, for high-speed load analyses, dynamic effects become significant and the assumption does not hold. Therefore, for future research is recommended to analyse the cycle based on the support's locations. In addition, more information can be obtained within the frequency domain. Therefore, for future research is recommended to move the analysis to the frequency domain as well and derive the dispersion curves.

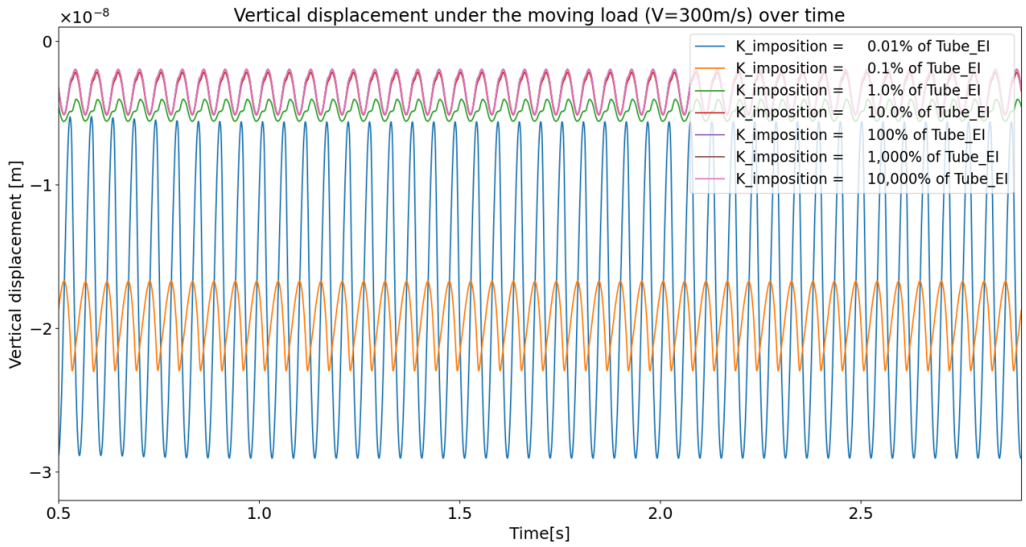


Figure 5.6: Vertical displacement with a moving load of 300 m/s for different stiffnesses of the imposition spring

**Vertical stiffness of the tube intersection spring (K_TubeIntersec)**
The intersection between the tube segments is represented by a vertical and rotational spring. An analysis is done to find the relation of the vertical spring's stiffness to the vertical displacement below the load. The rotational spring is set fixed in the analysis. In Figure 5.7, the displacement is plotted over time for a moving load with a velocity of 30 m/s. Only the pink line can be captured due to the same displacement patterns for the different stiffnesses at the tube intersection. This phenomenon applies also to the analyses with a velocity of 100 m/s and 300 m/s.

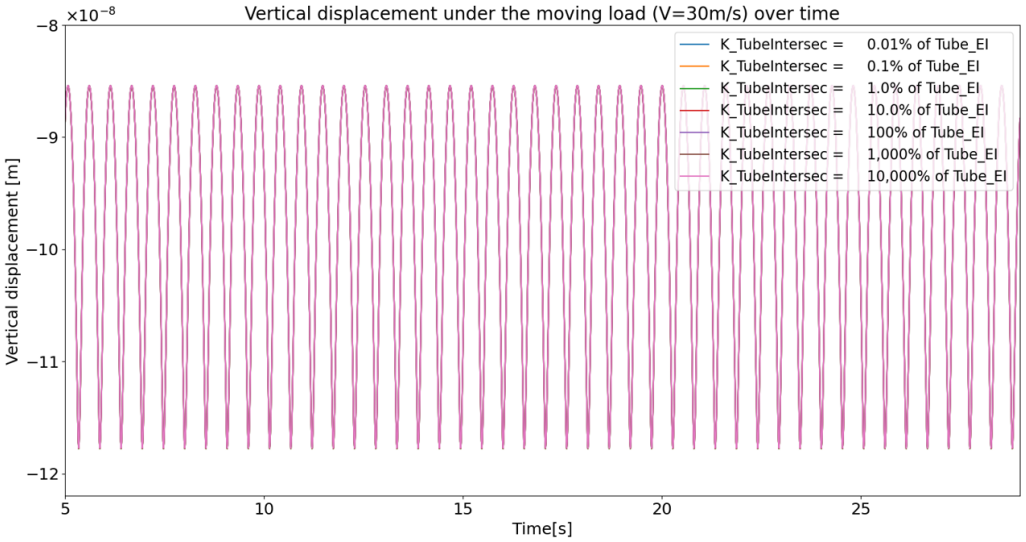


Figure 5.7: Vertical displacement with a moving load of 30 m/s for different vertical stiffnesses of the tube intersection

The analysis with a velocity of 300 m/s is shown in Figure 5.8 and has only a difference in the magnitude of displacement. The significantly lower displacement at 300 m/s indicates that the main critical velocity is below 300 m/s. About the influence of the tube intersection's stiffness on the displacement below the load, no certain statement can be made. The stiffness may be too high to see the difference, where the stiffness can be assumed infinite. Similar to the phenomenon in the analysis of the imposition spring, where the displacement ran to an asymptote.

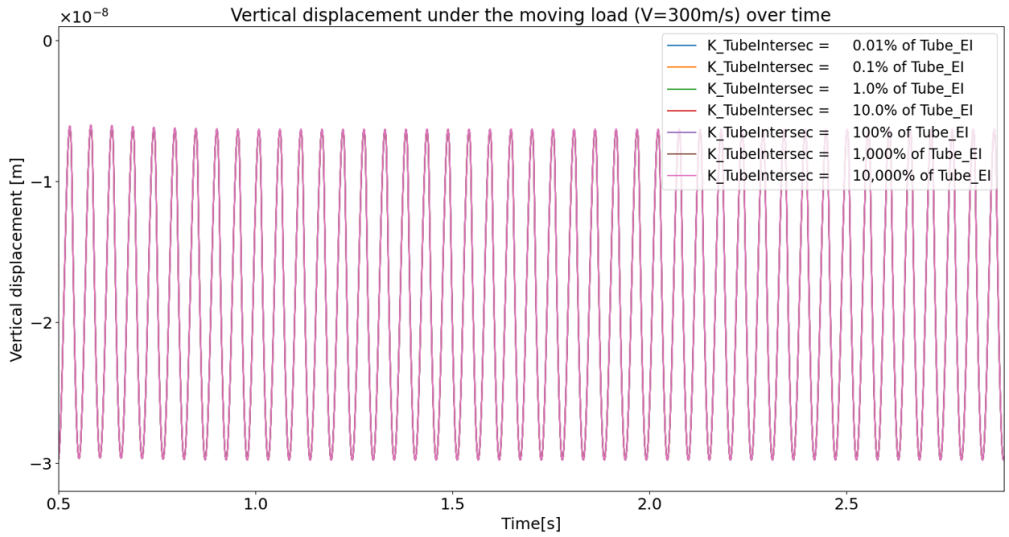


Figure 5.8: Vertical displacement with a moving load of 300 m/s for different vertical stiffnesses of the tube intersection

## 5.2 Displacement Difference between the Tube Segments

In addition to the vertical displacement of the tube below the load, the displacement difference at the tube intersections is pulled out of the model. The result shows the impact on the welded joints modelled by both a vertical and a rotational spring. A large displacement difference gives enormous stresses. The relative displacement with respect to the maximum displacement at the tube intersection is also considered to see if the displacement difference could be governing. The tube intersection could be the governing failure mode with a high relative displacement difference and a closer look is needed. The analyses are executed for three different stiffnesses with respect to the tube's bending stiffness for a moving load with both the velocity of 30 m/s and 300 m/s to find the influence on the tube intersection. This section focuses only on the relevant responses. An overview of all displacement difference plots is listed in Appendix C for completeness.

Figure 5.9 and 5.10 show the relation between the stiffness of the tube intersection spring and the displacement difference between the tube segments at the tube intersection when the pod is moving over the rail above the tube intersection for a pod velocity of 30 m/s and 300 m/s. The analysis is also executed for the imposition spring and the bending stiffness of the rail modelled as a beam. All stiffnesses have the same negative correlation: an increase in the stiffness of any spring or beam leads to a lower displacement difference between the tube segments independent of the pod's velocity. This principle holds across the whole operational velocity range. The reduction in displacement difference with increased stiffness occurs because stiffer components are more effective at resisting deformation and the movement of the tube segments is more constrained.

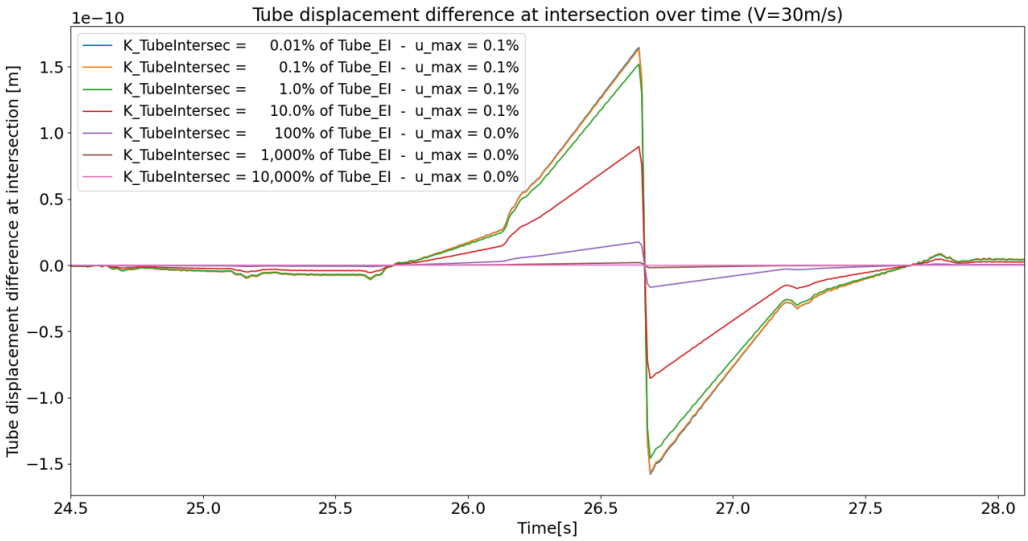


Figure 5.9: Displacement difference with a moving load of 30 m/s for different vertical stiffnesses of the tube intersection

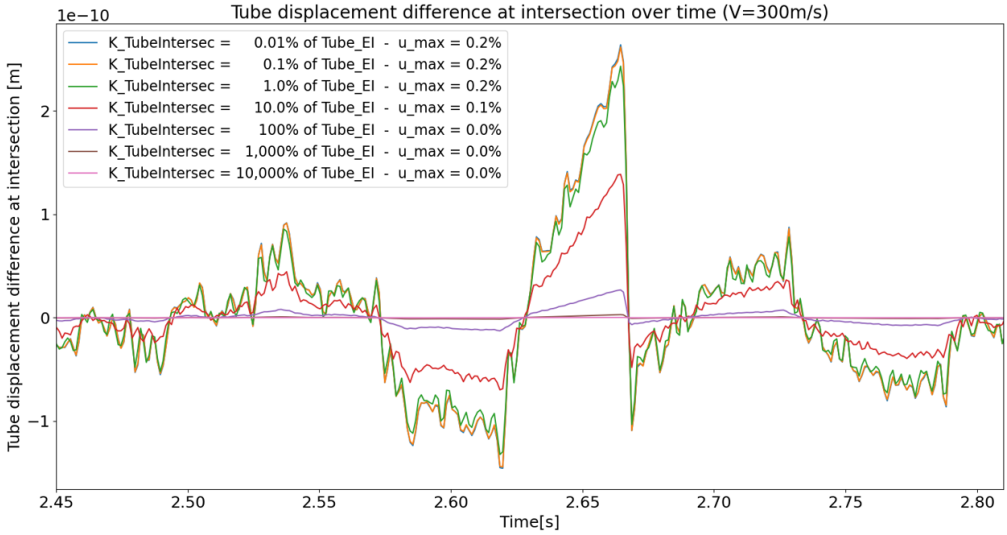


Figure 5.10: Displacement difference with a moving load of 300 m/s for different vertical stiffnesses of the tube intersection

The relation between the maximum displacement difference between the tube segments and the absolute displacement of the tube segment is different for the investigated springs. For the bending stiffness of the rail ($EI_{Rail}$) and the stiffness of the spring at the tube intersection ($K_{TubeIntersec}$) the relative displacement is always lower than 0.2%. For the stiffness of the imposition spring ($K_{imposition}$), the relative displacement can amount to 5.1% and could be the governing failure mode. Therefore, the imposition spring needs a closer look to exclude the displacement difference between tube segments as the governing failure mode.

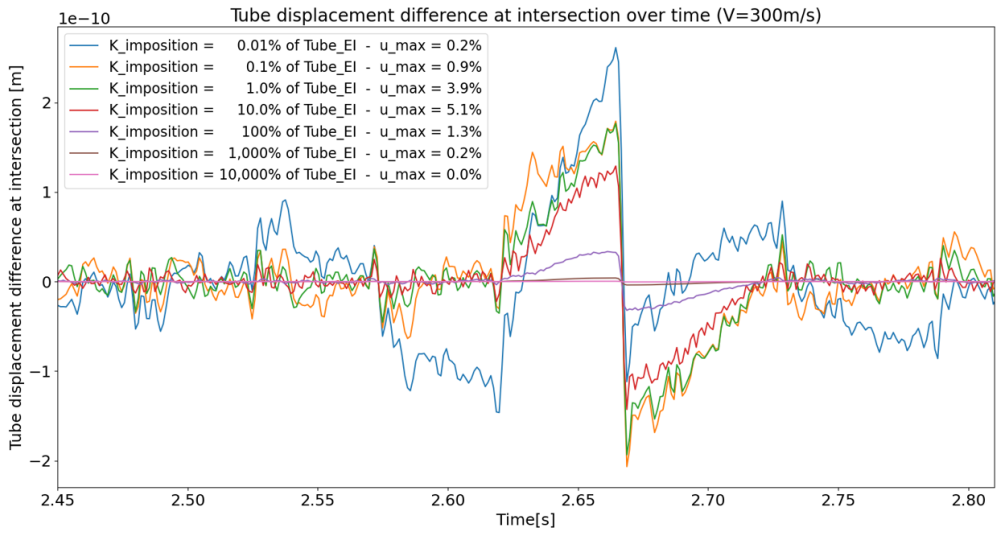


Figure 5.11: Displacement difference with a moving load of 300 m/s for different vertical stiffnesses of the tube intersection

Despite that the principles above hold across the whole operational velocity range, differences in the responses between pod velocities can be obtained. The response for the higher operational velocity has significantly more oscillations. The damping level could be too low, resulting in captured unrealistic oscillations. Therefore the damping value is investigated to exclude a possible source of the oscillations. Figure 5.12 shows the displacement difference for a random set of properties with different spring damping values relative to their stiffness. A small increase smooths the small oscillations and the higher damping values remove significant peaks, resulting in the loss of important information about the system. Both before and after the load has crossed the intersection, a crest and trough can be seen. These extrema are considered to be significant and caused by the system's dynamics since the extrema cannot be obtained for the analyses with a low pod velocity. Based on this damping analysis, the damping value does not have to be changed relative to the damping analysis executed in Section 3.5.

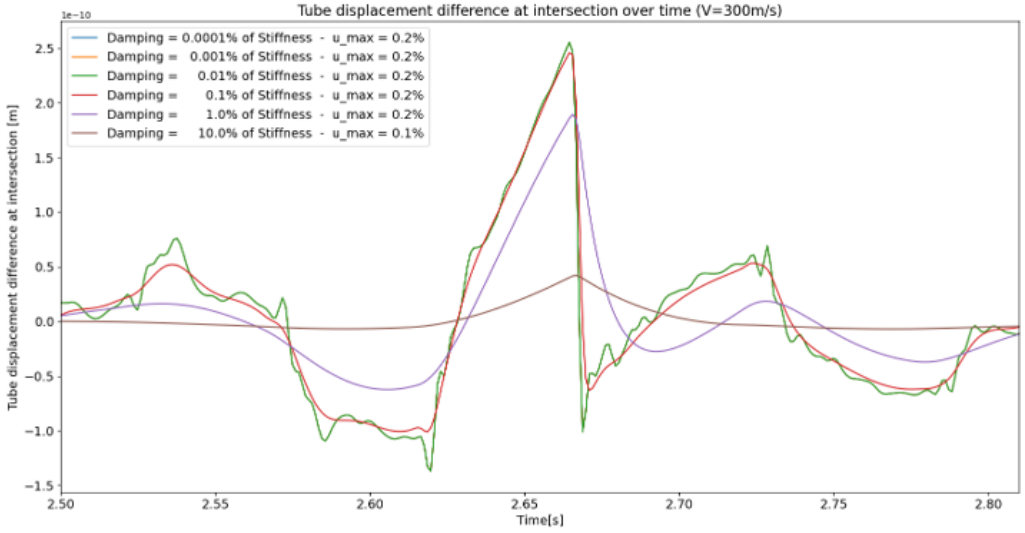


Figure 5.12: Displacement difference with a moving load of 300 m/s for different proportions of damping to the spring's stiffnesses

# 6 | Soil Influence

This chapter takes a closer look at the importance of soil inclusion in the finite element model by a literature study. The described models in Section 3.1 and 4.1 use a rigid foundation below the columns with the displacements set to zero. The fixed boundaries exclude coupling between the columns through the soil. The soil can directly affect the vibrational behaviour, stability and load-bearing capacity of the structure. Additionally, the soil is one of the most important external factors, which cannot be modified or changed. Therefore, soil properties are discussed to cover soil behaviour with a special focus on the soil parameters affecting the dynamic loading imposed by the moving pod within the Hyperloop system and their relations to the different wave speeds. Subsequently, the unique characteristics and challenges of the Dutch soil are taken into account. In the end, several model implementations are discussed to find the best implementation for the Dutch soil.

## 6.1 Soil Properties

The soil type is important in designing a structure. The mechanical properties linked to the soil type dictate how well the Hyperloop structure can support the imposed loads. Poorly analysed or insufficiently engineered soil can lead to undesired settlements or too much soil-structure interaction. The settlements could affect the alignment and smoothness of the track. Any misalignment can generate vibrations, leading to discomfort for the passengers and even threatening the structural integrity. The soil-structure interaction has influence on the dynamic response of the structure.

The key mechanical properties are based on two types of test: one to calculate the stress, strain and the other to calculate cohesion and the friction angle [46]. More about the tests and the relation of the measures to the soil properties can be found in Appendix D [47] [48]. Both described tests are executed with static loadings, resulting in no inclusion of wave propagation. For the Hyperloop case, taking into account propagation is essential to capture the soil-structure interaction. The coupling arises by the propagating waves travelling through both solids and interact through the structure's columns. The present mechanical waves in the soil can be divided into three groups by the direction of movement of the individual particles of the medium relative to the direction that the waves travel [49]:

- longitudinal waves
- Transverse waves
- Surface waves

The longitudinal waves can be described as pressure waves (P-waves), where the particles move in the material back and forth in the same direction as the wave is travelling. The transverse waves are called shear waves (S-waves), where the particles move perpendicular to the direction of wave propagation. Both type of waves have different wave velocities. The pressure waves move faster than the shear wave through the medium.

$$v_P = \sqrt{\frac{E(1-\nu)}{(1+\nu)(1-2\nu)\rho}} \quad ; \quad v_S = \sqrt{\frac{E}{2\rho(1+\nu)}} \tag{6.1}$$

The most profound surface wave is the Rayleigh wave. The wave moves in a circular motion, in both horizontal and vertical directions. The wave speed is related to the shear wave speed. The exact Rayleigh wave speed requires solving the characteristic equation numerically. An approximation is provided in Equation 6.2. The approximation is widely used due to its acceptable accuracy. For typical Poisson's ratio values of soil types, the Rayleigh wave speed is around 90% of the shear wave speed. The reduction in velocity is caused by energy dissipation at the surface and the involvement of both the vertical and horizontal particle motion.

$$v_R \approx v_S \cdot \left(\frac{0.862 + 1.14\nu}{1+\nu}\right) \tag{6.2}$$

The wave velocities do not directly indicate the wave's intensity but have a relation to the velocity of the moving pod. If the pod's velocity approaches the wave velocities, waves will be excited and the influence of the soil-structure interaction increases. Therefore, the wave speeds are preferred to be outside of the operational velocity range. All wave velocities are dependent on the following three soil parameters:

- Poisson ratio ($\nu$)
- Young's modulus ($E$)
- density ($\rho$)

The causations of the various parameters are analysed individually to understand their specific impact on wave speed values. During this process, other parameters are assigned standard values as reference values out of their typical ranges with a Poisson's ratio of 0.3, a Young's modulus of 50 MPa and a density of 1600 kg/m$^3$. These values represent common material properties for soils and ensure a controlled analysis of the influence of each variable on wave propagation.

As can be seen in Appendix D, the Poisson ratio measures the relation between the lateral and axial strains. The theoretical limits of Poisson's ratio are between -1 and 0.5. Soil types have a Poisson ratio from 0.2 for cohesionless soils to 0.5 for saturated clay soils. [50]. In the Poisson ratio range of the soil types is looked at the relation with the wave speed and shown in Figure 6.1. The speed of the pressure wave has a positive nonlinear relation with the Poison ratio. As Poisson's ratio approaches 0.5, the P-wave speed increases significantly, approaching infinity in theory, as materials with a Poisson ratio near 0.5 become nearly incompressible. In contrast, the shear wave (S-wave) and Rayleigh wave speeds demonstrate a more modest, negative linear relationship with Poisson's ratio. Despite the reduction in speed as Poisson's ratio increases, the proportion between S-wave and Rayleigh wave speeds remains nearly consistent.

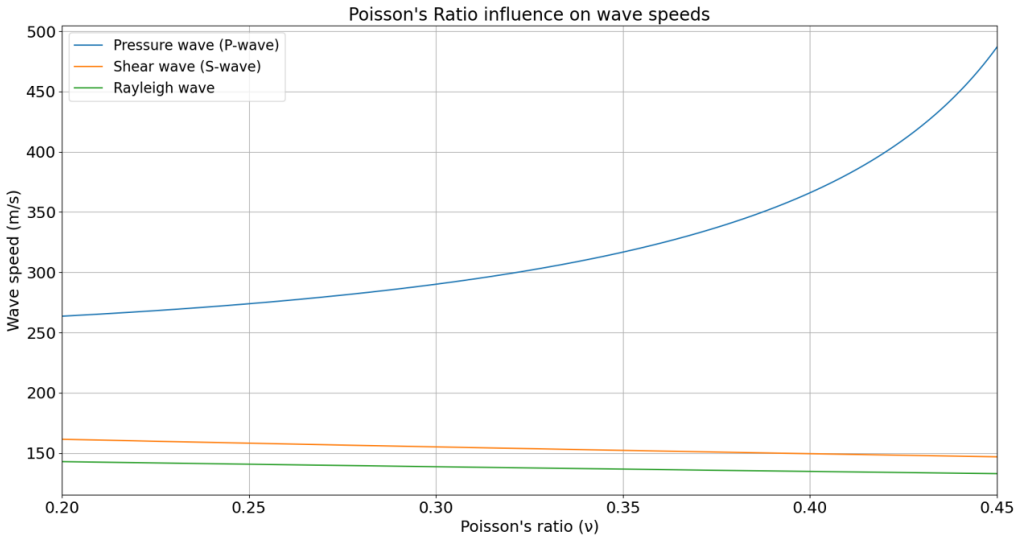


Figure 6.1: Influence of Poisson ratio on the wave speeds

The same analysis is executed for the relation between the Young's modulus and the wave speeds. The field values of the stress-strain modulus vary significantly per soil type due to several factors such as stress history and water content. Very soft clay has a Young's modulus between the 2 MPa and the 15 MPa, while the modulus for dense gravel between the 100 MPa and 200 MPa lies [50]. In Figure 6.2, the Young's modulus has a positive non-linear relation for all types of waves.

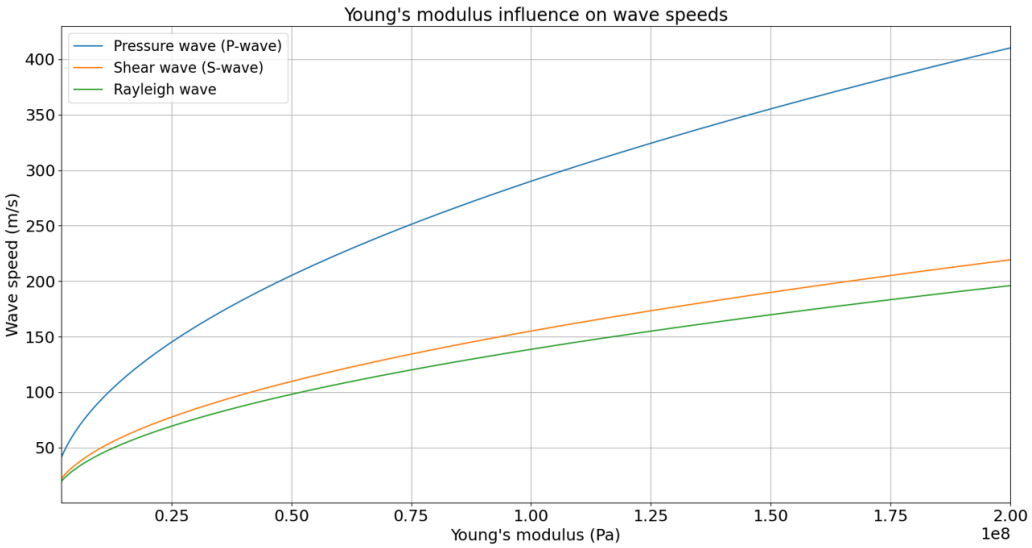


Figure 6.2: Influence of Young's modulus on the wave speeds

For the density in the relation between the density and the wave speeds, the field values are based on the dry unit weight [51]. To convert the unit weight into the density, the unit weight is divided by the gravitational constant ($g$). Resulting in a density range 800 - 2000 kg/m$^3$ for the different soil types. Figure 6.3 shows a negative non-linear relation. The proportions between the different types of waves stay for all parameters quite consistent.

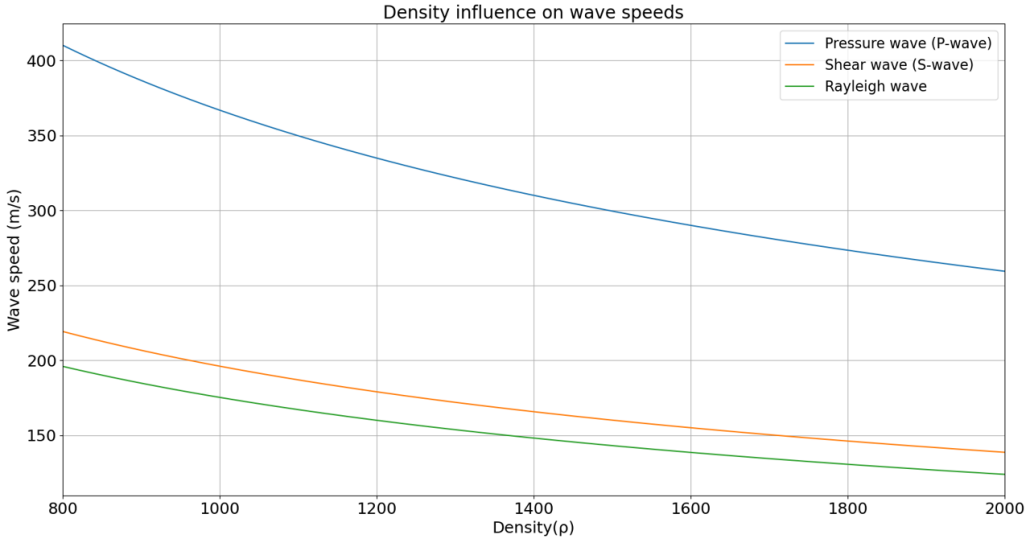


Figure 6.3: Influence of density on the wave speeds

## 6.2 Influences on Dutch Soil

The Dutch soil gives some unique geotechnical challenges due to the several types of soils. The combination of coastal, river and upland areas, together with human intervention leads to various soil types across the country shown in Figure 6.4. The greatest issues regarding these soil types are land subsidence, excessive settlement and salinization. All these factors demand careful geotechnical analyses to mitigate risks and ensure the stability of structures built on Dutch soil. This research focuses on the influence on the dynamic response's.

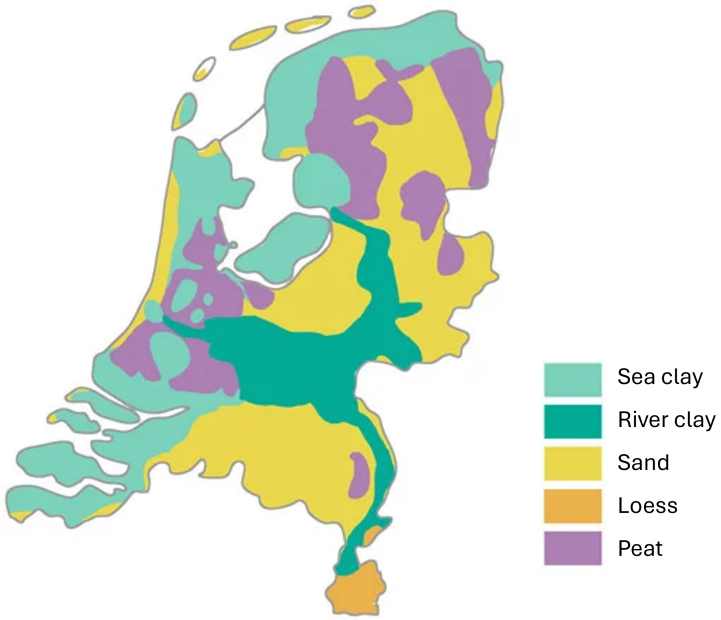


Figure 6.4: Soil types in the Netherlands [3]

In the Netherlands, the sand soil are well-drained and stable when compacted and therefore suitable for construction if properly managed. The soil types clay and peat are less advantageous for construction and need a closer look. Both types have a low Young's modulus and a high Poisson ratio with a drainage problem, making the types not the best for loaded structures. As mentioned in Section 6.1, a low Young's modulus leads to low wave speeds with a higher probability of being present within the operational velocity range of the moving pod. Additionally, the low Young's modulus results in a high compressibility and is therefore prone to settlements. The high Poisson ratio leads to lower shear and Rayleigh wave speeds, but a significantly higher pressure wave speed. Therefore the high lateral deformation under the load that is also present in the static case due to the high Poisson ratio is more significant.

## 6.3 Possible Model Implementations

A model is always a simplification of reality, aiming to approximate real-world conditions as closely as possible. In the finite element model in this research, the soil is represented with a zero-displacement boundary, meaning the soil at the boundary is fixed and can be seen as a spring with infinite stiffness. This simplification excludes the whole impact of the soil, resulting in no settlement or coupling between soil and structure. This chapter explains two soil implementations to represent the soil within the finite element model. The first implementation is a 2D modelled soil and the second is a shear beam representing the soil. Their method and adequacies and deficiencies are discussed to find the best implementation for Dutch soil. The implementation should improve accuracy and bridge the gap between the model and the response in reality. The more complex the implementation, the higher the computation time will be. The aim is to find the shortest computation time with acceptable accuracy. Therefore, a middle ground should be found to come up with the optimal solution.

The soil can be modelled as a 2-dimensional medium based on the conservation of momentum. The conservation of momentum is based on Newton's Second Law of Motion, stating the rate of change of momentum of an object is equal to the net force applied [52]. The inertia of the soil particles is neglected and the density and volume of the soil are assumed constant ($\frac{\partial \rho}{\partial t} = \frac{\partial Volume}{\partial t} = 0$). The momentum equation redistributes these forces throughout the soil domain, which can be calculated by the stresses and strains.

$$\rho \frac{\partial^2 w}{\partial^2 t} = \nabla \cdot \sigma \tag{6.3}$$

The stresses can be determined by the Lamé constants for a linear visco-elastic material together with the strains. The constants are dependent of Young's modulus and the Poisson ratio. The parameters can be substituted into the momentum equation. The equation of motion is shown in Equation 6.4 and can be used in the Finite element model. Where the equation is discretised into elements. In contrast to the beam and springs, the soil is modelled 2-dimensional. Therefore, the soil displacement is captured in both horizontal and vertical directions, increasing the computation time significantly.

$$\rho \frac{\partial^2 w}{\partial t^2} = (\lambda + G) \frac{\partial \bar{\varepsilon}}{\partial z} + G \nabla^2 w \tag{6.4}$$

Where,

- $\lambda = \frac{E\nu}{(1+\nu)(1-2\nu)}$
- $G = \frac{E}{2(1+\nu)}$
- $\bar{\varepsilon} = \varepsilon_x + \varepsilon_z$

Another possible approach to model the interaction between supports is to incorporate the soil-structure interaction through the addition of a shear beam beneath them. This method simplifies the soil from 2-dimensional to 1-dimensional by focusing mainly on the horizontal dynamics, capturing the coupling between the energy flow through the different columns. The waves can propagate in the shear beam and subsequently re-enter the Hyperloop structure at the adjacent support. The shear beam is assumed to transmit waves through shear deformation without bending, treating the beam as a non-dispersive medium. This assumption implies that the phase velocity remains constant for all frequencies and that the group velocity equals the phase velocity [52]. The phase velocity characterizes the speed of individual waves, while the group velocity describes the rate at which energy is transferred through these waves. As a result, shear waves can propagate with their original form without dispersion and facilitate a straightforward prediction of energy transfer between the structure and the soil. If the wave velocity within the shear beam equals the pod's velocity, the re-entered energy accumulates within the structure with an increased risk of instability. The vertical phenomena such as the elastic settlements are insufficiently represented due to challenges associated with the boundary conditions at the bottom of the shear beam. To simulate the soil as best as possible for a shear beam, a distributed foundation is preferable to capture some degree of settlement. Validation of the beam is essential to identify potential oversimplifications or unexpected responses that do not correspond to actual soil behaviour.

The shear beam is described by the equation of motion in Equation 6.5. The first two terms correspond to the shear beam itself, while the third and fourth terms account for the Winkler foundation beneath it. Parameter values should reflect the specific soil properties and can be calibrated using experimental data or existing models. The stiffness of the Winkler foundation can be based on the subgrade modulus ($k$).

$$\rho \frac{\partial^2 u}{\partial t^2} = G \frac{\partial^2 u}{\partial x^2} - ku - c \frac{\partial u}{\partial t} \tag{6.5}$$

# 7 | Conclusion and Recommendations

This research is conducted to find the dynamic response of a Hyperloop tube under the influence of a moving pod, considering various structural and soil parameters. The outcomes have provided insight into factors influencing the dynamic response of the Hyperloop tube, despite some obstacles not being overcome. In addition, the complexity of existing Hyperloop models has been increased and advanced methods are used within the models to improve the accuracy or computational efficiency. Therefore, the feasibility of modelling the Hyperloop system in a moving reference frame is investigated. Herein, steps are made to get reliable results out of the model without conquering all obstacles. This section discusses the identified obstacles and presents conclusions addressing the research questions outlined in Section 1.2, highlighted in bold. Each paragraph begins with a concise statement in italics, focused on answering the research question, followed by a detailed elaboration. In addition, a section with the model limitations is included. Throughout the chapter, potential improvements are discussed to provide future research recommendations for accurately representing the Hyperloop and providing a handle for overcoming the obstacles encountered in this research.

## 7.1 Conclusion

### I To what extent is a moving reference frame feasible for a moving load problem within a finite element model?

The moving reference frame can be implemented effectively to simulate the dynamic response of the moving pod over time if the numerical instability can be resolved. The influence on the computation time and accuracy of the model are explored together with the key considerations to find the feasibility of the moving reference frame's implementation for a moving load problem within a finite element model.

- **How does a moving reference frame influence the accuracy and computational efficiency for a moving load problem within a finite element model?**

  *A moving reference frame gives an increase in the computational efficiency without reducing the accuracy of the finite element model for a moving load problem, particularly for long transient analyses.*

  The domain size is a critical factor influencing the computation time. The spatial domain in a non-moving reference frame is dependent on the duration of the analyses. The longer the transient analysis, the greater the domain size. With the use of a moving reference frame, the domain is independent of the analysis duration and the domain can be restricted to the area of interest around the load. Therefore the computational efficiency is higher, the longer the duration of the transient analysis. The model's accuracy is preserved with the implementation of a moving reference frame, as identical methods are employed for the solution approximation and time and space discretization. Furthermore, the same area around the moving load is analysed. However, the validation of the model needs more attention, given that the moving boundaries may reflect propagating waves, potentially causing interference within the area of interest.

- **What are the key considerations for a stable implementation of a moving reference frame model for a moving load problem within a finite element model?**

  *The type of weighted residual method and the order of the discretisation are the key considerations for the stability of a moving reference frame within a finite element model for a moving load problem.*

  The least squares method should be implemented as the weighted residual method to transform the continuous equation of motions into discrete systems of algebraic equations. The method creates a symmetric system of algebraic equations, giving more stability to the model in comparison to the implementation of the standard Galerkin method. The time is discretised by the Newmark method which is an explicit method and unconditionally stable for the chosen parameters. With the least squares and Newmark method implemented in the finite element model, the steady-state analysis is stable with the moving reference frame implemented and validated for the continuously supported beam. The analysis does not have a time dependency and does not simulate the dynamic response of the moving pod in a finite element model over time. The transient analysis includes the time dependency, resulting in numerical instability problems which have not been resolved within the research due to the limited time frame.

Literature indicates the importance of the discretisation order. Future research is recommended to change the order of discretisation. The first discretisation should focus on the most critical discretisation. Since the discretisation of the time domain addresses the rapid changes in the transient analysis caused by the pod travelling at velocities of up to 300 m/s and the structure's geometry is modelled simply, the first discretisation should be in time. The recommended claim highlights the potential of the moving reference frame without guaranteeing stability.

## II What is the influence of the system's parameters on the dynamic response of the Hyperloop tube?

The influence of the system's parameters on the dynamic response of the Hyperloop tube is described by analysing the response of the vertical displacement under the moving load and the vertical displacement difference at the tube intersection for specific velocities. The influences of the pod's velocity and element stiffnesses are considered for both response types. In addition, the influence of different soil implementation types for the Dutch soil in a periodic supported model is discussed with a recommendation for future research.

- **What is the influence of the pod's velocity and the different element stiffnesses on the vertical displacement of the tube below the moving pod?**

*The different wave propagation regions are divided by one main critical velocity.*

Within the pod's operational velocities, resonance is observed in the parametric study. Despite theoretically having infinitely many critical velocities for periodically supported systems under the action of moving loads, the system considered in this research presents only one peak within the pod's operational velocity range. The significant amplification is called the main critical velocity. The relative velocity describes the system's behaviour because the interaction between the load and the structural dynamics of the system is incorporated and can be calculated by $v_{relative} = \frac{v_{pod}}{v_{critical}}$. The relative velocity normalises the results and indicates the different wave propagation regions. An increase in the pod's absolute velocity increases the pod's relative velocity with the possibility of encountering a shift in the wave propagation region. The shift gives a significantly different response of the vertical displacement of the tube below the moving load. The different wave propagation regions are divided by the main critical velocity:

$$\begin{cases} \text{If } v_{relative} < 1, \text{the displacement tends to stay constant for the different velocities,} \\ \text{If } v_{relative} = 1, \text{the displacement below the load has a significant amplification,} \\ \text{If } v_{relative} > 1, \text{the displacement decreases to zero for large relative velocities.} \end{cases}$$

Below the main critical velocity ($v_{relative} < 1$), the response acts in the quasi-static regime and no propagating waves influence the vertical displacement below the moving load. However, if the pod's velocity approaches the main critical velocity ($v_{relative} \to 1$), the system transitions into the moderate dynamic regime. In this regime, propagating waves interact with the vertical displacement beneath the moving load, causing an increasing dynamic amplification. This amplification reaches its peak when the pod's velocity matches the main critical velocity ($v_{relative} = 1$), a phenomenon referred to as the resonance regime. For the pod moving faster than the main critical speed ($v_{relative} > 1$), the response enters the high-speed regime. In this regime, the structure has insufficient time to react to the loading, causing the displacement to decrease to zero.

*The stiffness of the imposition spring and the tube's and rail's bending stiffness exhibit a positive correlation with the main critical velocity.*

The higher the (bending) stiffness, the higher the main critical velocity. Only the stiffness at the tube intersection has no influence on the main critical velocity. The positive relation is derived from the dynamic response of the set with the lowest stiffness values. In the analysis of the 'vertical displacement under the moving load', the pod's absolute velocity ($v_{pod}$) is held constant. The reduced displacement observed in the lowest stiffness set indicates a shift in the wave propagation regions. The phenomenon is associated to the region above the main critical velocity ($v_{relative} > 1$), contrasting with the other property sets, which are assumed to be to operate within the regime below the main critical velocity ($v_{relative} < 1$). By increasing the structure's stiffness, the likelihood of pushing the main critical velocity outside the operational range ($v_{relative} < 1$) becomes greater, which is desirable for ensuring stability and passenger comfort.

The current approach identifies the main critical velocity indirectly. A direct approach can be executed by plotting the displacement range against the pod's operational velocities as is done for the optimisation of the damping characteristics. The analysis is computationally heavy since the model has run for each operation velocity to find the displacement range for all pod's operational velocities. Despite the heavy computation, the plot is recommended for use in future research.

The question of which stiffness most significantly influences the dynamic response of the Hyperloop tube is not answered in this research because the non-dimensional parameter ($\alpha$) is not applied to all stiffnesses. Therefore the stiffnesses cannot be compared correctly. Future research should make the equation of motion dimensionless to find the non-dimensional parameters for the complex structure by scaling the parameters to remove their physical dimensions. The non-dimensional parameters should be utilized to compare the different parameters and identify the dominant effects.

The stiffnesses are analysed individually but the modelled springs and beams are connected, creating a dependency that cannot be neglected. Changing the stiffness of one spring influences the connected elements, eventually influencing the whole system. Even asymptotes are found in some analyses, indicating that a change in the stiffness no longer affects the system's behaviour and the parameter is no longer governing. To overcome the challenge of isolating the parameters, future research should add complexity less quickly and use more simplistic models to isolate the investigated factor more easily. So for testing the influence of the periodicity in future research, the response of a continuously supported beam should be compared to a periodically supported beam with the same set of properties.

- **What is the influence of different element stiffnesses on the displacement difference at a tube intersection?**

  *The displacement difference at the tube intersection has a negative relation with all elements' stiffness within the structure.*

  The negative relation is independent of the velocity and type of investigated element: the higher the (bending) stiffness, the lower the displacement difference at the tube intersection. In addition, the displacement difference with respect to the vertical displacement of the tube is not governing in most cases. Only in the analysis of the imposition spring, the value is 5.1% for one of the sets of properties and needs a closer look. All other stiffnesses have no values higher than 0.2%.

- **What is the influence of different soil implementation types for Dutch soil in a periodic supported model?**

  *The 2-dimensional soil captures the settlements in more detail than the shear beam implementation and should be implemented to represent the Dutch soil in future research.*

  The soil is modelled within the model as a fixed boundary due to limited research resources despite its significance on the dynamic response. All conclusions reported so far are based on the executed literature research. The important dynamic soil properties are the Poisson ratio ($\nu$), Young's modulus ($E$) and the density ($\rho$) of the soil. The three soil properties cover the dynamic response of the soil as they are the only variables in the wave speed equations. Despite that the wave velocities do not indicate the amount of energy propagating through the specific waves, the velocities are a good indicator for understanding the behaviour of the propagating waves in the soil. In addition, the 3 parameters can be used to model the 2-dimensional soil. The Dutch soil is known for its several different soil types within a small area, primarily clay and peat. Both types have a low Young's modulus, a high Poisson ratio and drainage issues, resulting in a high sensitivity to (elastic) settlements and lateral deformation under the load, meaning the soil compresses under the load but rebounds to its original state after the load is removed. Future research should model the soil as a 2-dimensional domain rather than a shear beam as the shear beam primarily emphasizes the soil-structure interaction by capturing the re-entering of the energy in the system, while the elastic soil settlements are significant in Dutch soils and better captured by the 2-dimensional soil implementation.

## 7.2 Model Limitations

The research is delineated to use the limited resources efficiently. Therefore, the model focuses on the Hyperloop concept above ground periodically supported. The representation of reality has several simplifications to reduce complexity and computation time, giving simultaneously model limitations. As a result, the rail is modelled as a continuous beam supported periodically by springs with infinite stiffnesses. The simplifications are assumed insignificant compared to the discontinuous tube supported periodically by spring with finite stiffnesses. The more significant simplifications are elaborated below with a recommendation to implement the simplification more accurately in future research.

**The Hyperloop system is built in a 2D space domain with 1D elements**
The Hyperloop system is modelled in a 2-dimensional space domain with only 1-dimensional elements, focusing on the vertical displacements. A straight Euler-Bernoulli beam without level changes represents the Hyperloop tube, excluding numerous inhomogeneities in the tube, referring to emergency exits, hubs and stations. As well as turns, switches and two-way pipes. The moving load is plotted as a point load representing a line load in the direction of the neglected dimension. The simplifications can lead to an unacceptable deviation from reality. The assessment of the structure's integrity can be improved by replacing the tube with a 3D shell structure. The representations include axial, shear and torsion deformation With the 3D model, the stability can be calculated in all directions and other load cases can be analysed correctly, such as accelerations of the pod or the wind forces acting on the structure. The same applies to other 1-dimensional elements, such as the springs representing the tube's columns.

**The column's span is fixed**
The periodicity impacts the overall vibration patterns of the Hyperloop system since the stiffness of the total structure becomes more inhomogeneous due to the stiffness injection at each column location. This research only focussed on the influence of the system's stiffness of the elements, keeping the column's span width fixed at 16 meters due to limited research time. In future research, the influence of the column's span should be investigated since the spacing and stiffness of the supports are the critical factors for the response of the system.

**The Hyperloop pod is represented by a moving constant load**
The representation of the Hyperloop pod excludes dynamic instability since the constant moving load cannot show the pod-tube interaction. The representation of the pod can be improved by a mass-spring system, which is a dynamic system with mass, stiffness and damping properties. The system can inject energy into the system by self-excitation effects. The interaction could be improved even further by modelling the magnetic forcing between the pod and tube.

**The model excludes non-linear geometric and material behaviour**
The model does not describe non-linear phenomena, excluding non-linear material behaviour under high loading, isotropic material properties and element irregularities. Therefore also no type of damage, such as fatigue, creep or corrosion, is present in the model. The rail is modelled continuous and periodic supported by the tube with infinitely stiff springs, assuming no deformation at the rail-tube interfaces. All supports are represented by springs, neglecting the mass of the supports. The mass of the Hyperloop pod is also neglected, resulting in no instability caused by the pod-structure interaction effects in which the magnetic interactions also are not included in the model. All the simplifications are made based on the assumption that the influences of the simplifications are insignificant to the influences of the effects included in the model.

# Bibliography


[1] Dennis Kuiper, Materthesis_hyperloop: The dynamic response of a hyperloop tube, (2024).

[2] Hardt Hyperloop, Hyperloop progress paper, August 2023, page 29.

[3] Florum BV, Grondsoorten in nederland, (2024).

[4] Open Access Government, The European transport sector must innovate to remain competitive, (2019).

[5] Elon Musk, Hyperloop alpha, *SpaceX*, (2013).

[6] Konstantinos Gkoumas, Hyperloop academic research: A systematic review and a taxonomy of issues, *Applied Sciences*, (2021), 11(13).

[7] Nicholas Alexander and Mohammad Kashani, Exploring bridge dynamics for ultra-high-speed, hyperloop, trains, *Structures*, 03 2018, 14:69–74.

[8] Ehsan Ahmadi, Mohammad Kashani, and Nicholas Alexander, Dynamic amplification factors for ultra-high-speed hyperloop trains: Vertical and lateral vibrations, In: *Proc.* , 09 2020.

[9] Andrei B. Fărăgău, Andrei V. Metrikine, and Karel N. van Dalen, Dynamic amplification in a periodic structure subject to a moving load passing a transition zone: Hyperloop case study, In: *Proc. Recent Trends in Wave Mechanics and Vibrations*, eds, Dimitrovová, Zuzana and Biswas, Paritosh and Gonçalves, Rodrigo and Silva, Tiago, Cham, (2023). Springer International Publishing, 651–661.

[10] Tao Lu, Shuxuan Yuan, Tianyu Wang, Xiang Liu, Ping Wang, and Rong Chen, Dynamic response and wave motion of a periodically supported beam under an ultra-high-speed load: Wave dispersion and critical velocities, *International Journal of Solids and Structures*, (2024), 291:112694.

[11] Pedro Museros, Carlos Lázaro, Benjamín Pinazo, and Salvador Monleón, Key aspects in the analysis and design of hyperloop™ infrastructure under static, dynamic and thermal loads, *Engineering Structures*, (2021), 239.

[12] Ladislav Frýba, Vibration of solids and structures under moving loads, In: *Proc.* , Springer Dordrecht, (1973).

[13] A.V. Vostroukhov and A.V. Metrikine, Periodically supported beam on a visco-elastic layer as a model for dynamic analysis of a high-speed railway track, *International Journal of Solids and Structures*, (2003), 40(21):5723–5752.

[14] M. Botshekan, M. Tootkaboni, and A. Louhghalam, On the dynamics of periodically restrained flexural structures under moving loads, *International Journal of Solids and Structures*, (2019), 180-181:62–71.

[15] Abdusamad A Salih, Finite element method, *Department of Aerospace Engineering Indian Institute Of Space Science And Technology Thiruvananthapuram-*, (2012).

[16] Stephen P. Timoshenko and James M. Gere, Theory of elastic stability, In: *Proc.* , *Recent Trends in Wave Mechanics and Vibrations*. McGraw-Hill International Book Company, (1963).

[17] J.M. Gere and S.P. Timoshenko, *Mechanics of Materials*, Stanley Thornes, (1999).

[18] Ray W. Clough and Joseph Penzien, *Dynamics of Structures*, McGraw-Hill, New York, second edition, (1993).

[19] Boris G. Galerkin, Series solution of some problems of elastic equilibrium of rods and plates, *Vestnik Inzhenerov i Tekhnikov*, (1915), 19:897–908.

[20] L. Andersen, S.R.K. Nielsen, and P.H. Kirkegaard, Finite element modelling of infinite euler beams on kelvin foundations exposed to moving loads in convected co-ordinates, *Journal of Sound and Vibration*, (2001), 241(4):587–604.

[21] Kok Keng Ang and Jian Dai, Response analysis of high-speed rail system accounting for abrupt change of foundation stiffness, *Journal of Sound and Vibration*, (2013), 332(12):2954–2970.

[22] Diego Froio, Egidio Rizzi, Fernando Simões, and António Pinto da Costa, A true pml approach for steady-state vibration analysis of an elastically supported beam under moving load by a dlsfem formulation, *Computers Structures*, 10 2020, 239:106295.

[23] Rakesh Ranjan and J Reddy, Non uniform rational bspline (nurbs) based non-linear analysis of straight beams with mixed formulations, *Journal of Solid Mechanics*, 12 2016, 8.

[24] Cody C. Rasmussen, The least-squares finite element method applied to fluid-structure interaction problems, Master's thesis, University of Wyoming, (2011).

[25] Eleni Chatzi, The finite element method for the analysis of non-linear and dynamic systems: Non-linear dynamics part i, In: *Proc.* , (2017).

[26] Alexander F. Shchepetkin, An adaptive, courant-number-dependent implicit scheme for vertical advection in oceanic modeling, *Ocean Modelling*, (2015), 91:38–69.

[27] Nathan M. Newmark, A method of computation for structural dynamics, *Journal of the Engineering Mechanics Division*, (1959), 85(3):67–94.

[28] Vu-Hieu Nguyen and Denis Duhamel, Finite element procedures for nonlinear structures in moving coordinates. part ii: Infinite beam under moving harmonic loads, *Computers Structures*, 11 2008, 86.

[29] Brown University, Dynamics and vibrations: Notes, `https://www.brown.edu/academics/engineering/courses/en224/dynamics_and_vibrations/`.

[30] Dennis Klerk, Daniel Rixen, and Sven Voormeeren, General framework for dynamic substructuring: History, review, and classification of techniques, *Aiaa Journal - AIAA J*, 05 2008, 46:1169–1181.

[31] João Manuel de Oliveira Barbosa and Karel N. van Dalen, Dynamic response of an infinite beam periodically supported by sleepers resting on a regular and infinite lattice: Semi-analytical solution, *Journal of Sound and Vibration*, (2019), 458:276–302.

[32] T.J.R. Hughes, *The Finite Element Method: Linear Static and Dynamic Finite Element Analysis*, Dover Publications, (2012).

[33] William H. Press, Saul A. Teukolsky, William T. Vetterling, and Brian P. Flannery, *Numerical Recipes: The Art of Scientific Computing*, Cambridge University Press, 3rd edition, (2007).

[34] Andrei Fărăgău and Karel N. van Dalen, MovingLoadDynamics_CanonicalProblem4, CIEM5220 Applied Dynamics of Structures, TU Delft, (2023), MatLab file.

[35] A.W.M. Kok, Finite element models for the steady state analysis of moving loads, *Heron, 45 (1), 2000*, 01 2000, 45.

[36] B.N. Jiang, *The Least-Squares Finite Element Method*, Springer-Verlag New York, Inc., Heidelberg, NY, (1998).

[37] Seong-Min Kim and Jose M. Roesset, Dynamic response of a beam on a frequency-independent damped elastic foundation to moving load, *Journal of Engineering Mechanics*, (2003), 129(2):206–216.

[38] Rupen Basu and G. V. Rao, Analytical solutions for euler-bernoulli beam on viscoelastic foundation subjected to moving load, *Journal of Sound and Vibration*, (2006), 290(3-5):1283–1293.

[39] J.T. Kenney, Steady-state vibrations of beam on elastic foundation for moving load, *Journal of Applied Mechanics*, (1954).

[40] V.Z. Vlasov and U.N. Leont'ev, *Beams, Plates and Shells on Elastic Foundations*, Israel Program for Scientific Translations Ltd., Jerusalem, Israel, (1966).

[41] Ameeta Amar Raut, Nonlinear analysis of beams using least-squares finite element models based on the euler-bernoulli and timoshenko beam theories, Master's thesis, Texas A&M University, College Station, TX, December 2009, Major: Mechanical Engineering.

[42] A. V. Metrikine and A. R. M. Wolfert, Steady-state response of periodically supported structures to a moving load, *European Journal of Mechanics - A/Solids*, (1999), 18(4):679–701.

[43] Jean Donea and Antonio Huerta, *Finite Element Methods for Flow Problems*, John Wiley & Sons, (2003).

[44] R.J. van Leijden, Parametric instability of an oscillator moving on a railway track, Master's thesis, Delft University of Technology, September 2021, Master's thesis in Civil Engineering & Geosciences.

[45] V. L. Ginzburg and V. N. Tsytovich, Transition radiation and transition scattering - Some questions regarding the theory, *Moscow Izdatel Nauka*, (1984).

[46] Arnold Verruijt, *An Introduction to Soil Mechanics*, Springer, (2017).

[47] Karl Terzaghi, *Theoretical Soil Mechanics*, Wiley, New York, (1943).

[48] Ludwig Prandtl, Über die härte plastischer körper, *Nachrichten von der Gesellschaft der Wissenschaften zu Göttingen, Mathematisch-Physikalische Klasse*, (1920).

[49] The Physics Classroom, Categories of waves, (2023).

[50] Joseph E. Bowles, *Foundation Analysis and Design*, McGraw-Hill, New York, (1996).

[51] Braja M. Das, *Principles of Geotechnical Engineering*, Cengage Learning, Stamford, CT, 7th edition, (2010).

[52] F. E. Richart, J. R. Hall, and R. D. Woods, *Vibrations of Soils and Foundations*, Prentice-Hall, Englewood Cliffs, NJ, (1970).

# A Galerkin Method

## A.1 Calculate Shape Functions

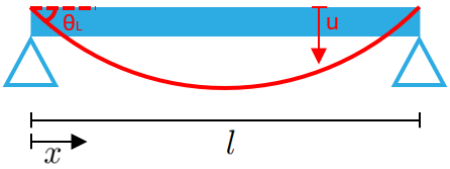


$u(x=0) = u_L$
$\theta(x=0) = \theta_L$
$u(x=l) = u_R$
$\theta(x=l) = \theta_R$

$$u(x) \approx \underbrace{\begin{bmatrix} N_1(x) & N_2(x) & N_3(x) & N_4(x) \end{bmatrix}}_{\mathbf{N}(x)} \begin{bmatrix} u_l \\ \theta_l \\ u_r \\ \theta_r \end{bmatrix} = \mathbf{N}(x)\mathbf{u}$$

$$\begin{bmatrix} N_1(0) & N_2(0) & N_3(0) & N_4(0) \\ N_1'(0) & N_2'(0) & N_3'(0) & N_4'(0) \\ N_1(l) & N_2(l) & N_3(l) & N_4(l) \\ N_1'(l) & N_2'(l) & N_3'(l) & N_4'(l) \end{bmatrix} \begin{bmatrix} u_L \\ \theta_L \\ u_R \\ \theta_R \end{bmatrix} = \begin{bmatrix} u_L \\ \theta_L \\ u_R \\ \theta_R \end{bmatrix} => \begin{bmatrix} 1 & 0 & 0 & 0 \\ 0 & 1 & 0 & 0 \\ 0 & 0 & 1 & 0 \\ 0 & 0 & 0 & 1 \end{bmatrix} \begin{bmatrix} u_L \\ \theta_L \\ u_R \\ \theta_R \end{bmatrix} = \begin{bmatrix} u_L \\ \theta_L \\ u_R \\ \theta_R \end{bmatrix}$$

The shape functions are approximated by a polynomial of the third order:
$N(x) = A + Bx + Cx^2 + Dx^3$
$N'(x) = B + 2Cx + 3Dx^2$

First column:

$$\begin{bmatrix} N_1(0) \\ N_1'(0) \\ N_1(l) \\ N_1'(l) \end{bmatrix} = \begin{bmatrix} 1 \\ 0 \\ 0 \\ 0 \end{bmatrix} \Rightarrow \begin{matrix} A_1 + B_1 \cdot 0 + C_1 \cdot 0^2 + D_1 \cdot 0^3 = 1 \\ 0 + B_1 + 2C_1 \cdot 0 + 3D_1 \cdot 0^2 = 0 \\ A_1 + B_1 \cdot l + C_1 \cdot l^2 + D_1 \cdot l^3 = 0 \\ 0 + B_1 + 2C_1 \cdot l + 3D_1 \cdot l^2 = 0 \end{matrix} \Rightarrow \begin{bmatrix} 1 & 0 & 0 & 0 \\ 0 & 1 & 0 & 0 \\ 1 & l & l^2 & l^3 \\ 0 & 1 & 2l & 3l^2 \end{bmatrix} \begin{bmatrix} A_1 \\ B_1 \\ C_1 \\ D_1 \end{bmatrix} = \begin{bmatrix} 1 \\ 0 \\ 0 \\ 0 \end{bmatrix} \Rightarrow \begin{bmatrix} A_1 \\ B_1 \\ C_1 \\ D_1 \end{bmatrix} = \begin{bmatrix} 1 \\ 0 \\ -\frac{3}{l^2} \\ \frac{2}{l^3} \end{bmatrix}$$

Second column:

$$\begin{bmatrix} N_2(0) \\ N_2'(0) \\ N_2(l) \\ N_2'(l) \end{bmatrix} = \begin{bmatrix} 0 \\ 1 \\ 0 \\ 0 \end{bmatrix} \Rightarrow \begin{matrix} A_2 + B_2 \cdot 0 + C_2 \cdot 0^2 + D_2 \cdot 0^3 = 0 \\ 0 + B_2 + 2C_2 \cdot 0 + 3D_2 \cdot 0^2 = 1 \\ A_2 + B_2 \cdot l + C_2 \cdot l^2 + D_2 \cdot l^3 = 0 \\ 0 + B_2 + 2C_2 \cdot l + 3D_2 \cdot l^2 = 0 \end{matrix} \Rightarrow \begin{bmatrix} 1 & 0 & 0 & 0 \\ 0 & 1 & 0 & 0 \\ 1 & l & l^2 & l^3 \\ 0 & 1 & 2l & 3l^2 \end{bmatrix} \begin{bmatrix} A_2 \\ B_2 \\ C_2 \\ D_2 \end{bmatrix} = \begin{bmatrix} 0 \\ 1 \\ 0 \\ 0 \end{bmatrix} \Rightarrow \begin{bmatrix} A_2 \\ B_2 \\ C_2 \\ D_2 \end{bmatrix} = \begin{bmatrix} 0 \\ 1 \\ -\frac{2}{l} \\ \frac{1}{l^2} \end{bmatrix}$$

Third column:

$$\begin{bmatrix} N_3(0) \\ N_3'(0) \\ N_3(l) \\ N_3'(l) \end{bmatrix} = \begin{bmatrix} 0 \\ 0 \\ 1 \\ 0 \end{bmatrix} \Rightarrow \begin{matrix} A_3 + B_3 \cdot 0 + C_3 \cdot 0^2 + D_3 \cdot 0^3 = 0 \\ 0 + B_3 + 2C_3 \cdot 0 + 3D_3 \cdot 0^2 = 0 \\ A_3 + B_3 \cdot l + C_3 \cdot l^2 + D_3 \cdot l^3 = 1 \\ 0 + B_3 + 2C_3 \cdot l + 3D_3 \cdot l^2 = 0 \end{matrix} \Rightarrow \begin{bmatrix} 1 & 0 & 0 & 0 \\ 0 & 1 & 0 & 0 \\ 1 & l & l^2 & l^3 \\ 0 & 1 & 2l & 3l^2 \end{bmatrix} \begin{bmatrix} A_3 \\ B_3 \\ C_3 \\ D_3 \end{bmatrix} = \begin{bmatrix} 0 \\ 0 \\ 1 \\ 0 \end{bmatrix} \Rightarrow \begin{bmatrix} A_3 \\ B_3 \\ C_3 \\ D_3 \end{bmatrix} = \begin{bmatrix} 0 \\ 0 \\ \frac{3}{l^2} \\ -\frac{2}{l^3} \end{bmatrix}$$

Fourth column:

$$\begin{bmatrix} N_4(0) \\ N_4'(0) \\ N_4(l) \\ N_4'(l) \end{bmatrix} = \begin{bmatrix} 0 \\ 0 \\ 0 \\ 1 \end{bmatrix} \Rightarrow \begin{matrix} A_4 + B_4 \cdot 0 + C_4 \cdot 0^2 + D_4 \cdot 0^3 = 0 \\ 0 + B_4 + 2C_4 \cdot 0 + 3D_4 \cdot 0^2 = 0 \\ A_4 + B_4 \cdot l + C_4 \cdot l^2 + D_4 \cdot l^3 = 0 \\ 0 + B_4 + 2C_4 \cdot l + 3D_4 \cdot l^2 = 1 \end{matrix} \Rightarrow \begin{bmatrix} 1 & 0 & 0 & 0 \\ 0 & 1 & 0 & 0 \\ 1 & l & l^2 & l^3 \\ 0 & 1 & 2l & 3l^2 \end{bmatrix} \begin{bmatrix} A_4 \\ B_4 \\ C_4 \\ D_4 \end{bmatrix} = \begin{bmatrix} 0 \\ 0 \\ 0 \\ 1 \end{bmatrix} \Rightarrow \begin{bmatrix} A_4 \\ B_4 \\ C_4 \\ D_4 \end{bmatrix} = \begin{bmatrix} 0 \\ 0 \\ -\frac{1}{l} \\ \frac{1}{l^2} \end{bmatrix}$$

$$N(x) = A + Bx + Cx^2 + Dx^3 => \begin{bmatrix} N_1 \\ N_2 \\ N_3 \\ N_4 \end{bmatrix} = \begin{bmatrix} A_1 & B_1 & C_1 & D_1 \\ A_2 & B_2 & C_2 & D_2 \\ A_3 & B_3 & C_3 & D_3 \\ A_4 & B_4 & C_4 & D_4 \end{bmatrix} \begin{bmatrix} 1 \\ x \\ x^2 \\ x^3 \end{bmatrix} = \begin{bmatrix} 1 & 0 & -\frac{3}{l^2} & \frac{2}{l^3} \\ 0 & 1 & -\frac{3}{l^2} & \frac{2}{l^3} \\ 0 & 0 & \frac{3}{l^2} & -\frac{2}{l^3} \\ 0 & 0 & -\frac{1}{l^2} & \frac{1}{l^3} \end{bmatrix} \begin{bmatrix} 1 \\ x \\ x^2 \\ x^3 \end{bmatrix}$$

## A.2 Calculate Matrices

$\int_0^L \mathbf{N}(\mathbf{x})^T R_s(x)\, dx = 0$

$R_s(x) = m\mathbf{N}(x)\ddot{\mathbf{u}} + EI\mathbf{N}''''(x)\mathbf{u} - f$

$W_i(x) = N_i(x)$
$i = 1, 2, 3, 4$

$$\int_0^L \begin{bmatrix} N_1 \\ N_2 \\ N_3 \\ N_4 \end{bmatrix} R_s(x)\, dx = \begin{bmatrix} 0 \\ 0 \\ 0 \\ 0 \end{bmatrix} => \int_0^L \mathbf{N}^T \left( m\ddot{\mathbf{N}} + EI\mathbf{N}''''\mathbf{u} - f \right) dx = 0$$

$m \int_0^L \mathbf{N}^T\mathbf{N}\, dx\, \ddot{\mathbf{u}} + EI \int_0^L \mathbf{N}^T\mathbf{N}''''\, dx\, \mathbf{u} - \int_0^L \mathbf{N}^T f\, dx = 0$ :

- $m \int_0^L \mathbf{N}^T\mathbf{N}\, dx = m \int_0^L \begin{bmatrix} N_1 \\ N_2 \\ N_3 \\ N_4 \end{bmatrix} \begin{bmatrix} N_1 & N_2 & N_3 & N_4 \end{bmatrix} dx = \frac{mL}{420} \begin{bmatrix} 156 & 22L & 54 & -13L \\ 22L & 4L^2 & 13L & -3L^2 \\ 54 & 13L & 156 & -22L \\ -13L & -3L^2 & -22L & 4L^2 \end{bmatrix} = \mathbf{M}\ddot{\mathbf{u}}$
- $EI \int_0^L \mathbf{N}''''\mathbf{N}\, dx\, \mathbf{u} = EI\mathbf{N}^T\mathbf{N}''''\Big|_0^L \mathbf{u} - EI \int_0^L \mathbf{N}''\mathbf{N}^T\, dx\, \mathbf{u} = EI\mathbf{N}^T\mathbf{N}'''\Big|_0^L \mathbf{u} - EI\mathbf{N}^T\mathbf{N}''\Big|_0^L \mathbf{u} + EI \int_0^L \mathbf{N}''^T\mathbf{N}''\, dx\, \mathbf{u}$
  - $EI\mathbf{N}^T\mathbf{N}'''\Big|_0^L \mathbf{u} = EI\left(\mathbf{N}(L)^T\mathbf{N}'''(L)\mathbf{u} - \mathbf{N}(0)^T\mathbf{N}'''(0)\mathbf{u}\right) = \begin{bmatrix} 0 \\ 0 \\ 1 \\ 0 \end{bmatrix} EI\, u''(L) - \begin{bmatrix} 1 \\ 0 \\ 0 \\ 0 \end{bmatrix} EI\, u''(0) = \begin{bmatrix} V_l \\ 0 \\ -V_r \\ 0 \end{bmatrix}$
  - $EI\mathbf{N}^T\mathbf{N}'''\Big|_0^L \mathbf{u} = EI\left(\mathbf{N}'(L)^T\mathbf{N}'''(L)\mathbf{u} - \mathbf{N}'(0)^T\mathbf{N}'''(0)\mathbf{u}\right) = \begin{bmatrix} 0 \\ 0 \\ 0 \\ 1 \end{bmatrix} EI\, u''(L) - \begin{bmatrix} 0 \\ 1 \\ 0 \\ 0 \end{bmatrix} EI\, u''(0) = \begin{bmatrix} 0 \\ -M_l \\ 0 \\ M_r \end{bmatrix}$
  - $EI \int_0^L \mathbf{N}''^T\mathbf{N}''\, dx = EI \begin{bmatrix} \frac{12}{L^3} & \frac{6}{L^2} & -\frac{12}{L^3} & \frac{6}{L^2} \\ \frac{6}{L^2} & \frac{4}{L} & -\frac{6}{L^2} & \frac{2}{L} \\ -\frac{12}{L^3} & -\frac{6}{L^2} & \frac{12}{L^3} & -\frac{6}{L^2} \\ \frac{6}{L^2} & \frac{2}{L} & -\frac{6}{L^2} & \frac{4}{L} \end{bmatrix} = \mathbf{K} = \mathbf{C}$

$$\begin{bmatrix} V_l \\ 0 \\ -V_r \\ 0 \end{bmatrix} - \begin{bmatrix} 0 \\ M_l \\ 0 \\ -M_r \end{bmatrix} + EI \begin{bmatrix} \frac{12}{L^3} & \frac{6}{L^2} & -\frac{12}{L^3} & \frac{6}{L^2} \\ \frac{6}{L^2} & \frac{4}{L} & -\frac{6}{L^2} & \frac{2}{L} \\ -\frac{12}{L^3} & -\frac{6}{L^2} & \frac{12}{L^3} & -\frac{6}{L^2} \\ \frac{6}{L^2} & \frac{2}{L} & -\frac{6}{L^2} & \frac{4}{L} \end{bmatrix} \mathbf{u} = \mathbf{K}\mathbf{u} + \begin{bmatrix} V_l \\ M_l \\ -V_r \\ -M_r \end{bmatrix}$$

- For point load ($f(x) = F_0\, \delta(x - x_0)$) $=> \int_0^L \mathbf{N}^T f\, dx = F_0 \begin{bmatrix} N_1(x_0) \\ N_2(x_0) \\ N_3(x_0) \\ N_4(x_0) \end{bmatrix} = \begin{bmatrix} F_l \\ M_l \\ F_r \\ M_r \end{bmatrix}$

$$\mathbf{M} \begin{bmatrix} \ddot{u}_l \\ \ddot{\theta}_l \\ \ddot{u}_r \\ \ddot{\theta}_r \end{bmatrix} + \mathbf{C} \begin{bmatrix} \dot{u}_l \\ \dot{\theta}_l \\ \dot{u}_r \\ \dot{\theta}_r \end{bmatrix} + \mathbf{K} \begin{bmatrix} u_l \\ \theta_l \\ u_r \\ \theta_r \end{bmatrix} = f, \text{ where } f = \begin{bmatrix} F_{l,ext} \\ M_{l,ext} \\ F_{r,ext} \\ M_{r,ext} \end{bmatrix} + \begin{bmatrix} V_l \\ M_l \\ -V_r \\ -M_r \end{bmatrix}$$

# B Least Squares Method

```
> restart;
Least Square Method: Mixed formulation in moving reference frame
> X1 := -diff(M(x,t),x,x) - m*v^2*M(x,t)/EI - 2*m*v*diff(W(x,t),x,t) + m*diff(W(x,t),t,t) + c*diff(W(x,t),t) - c*v*diff(W(x,t),x) + k
      *W(x,t) - p:
> X2 := M(x,t) + EI*diff(W(x,t),x,x):

unknowns in terms of shape functions
> We(x,t) := N1(x)*W1(t) + N2(x)*W2(t) + N3(x)*W3(t) + N4(x)*W4(t)
                We := (x,t) -> N1(x)*W1(t) + N2(x)*W2(t) + N3(x)*W3(t) + N4(x)*W4(t)   (1)
> Me(x,t) := N1(x)*M1(t) + N2(x)*M2(t) + N3(x)*M3(t) + N4(x)*M4(t)
                Me := (x,t) -> N1(x)*M1(t) + N2(x)*M2(t) + N3(x)*M3(t) + N4(x)*M4(t)   (2)

Residuals
> R1 := expand(subs([W(x,t) = We(x,t), M(x,t) = Me(x,t)], X1)):
> R2 := expand(subs([W(x,t) = We(x,t), M(x,t) = Me(x,t)], X2)):

Applying LSM method:
  - Take derivative of the residual towards one unknown
  - Multiplying with the original residual
  - Sum up the two terms
> W1 := expand(diff(R1,W1)*R1*p1 + p2*diff(R2,W1)*R2):
> W2 := expand(diff(R1,W2)*R1*p1 + p2*diff(R2,W2)*R2):
> W3 := expand(diff(R1,W3)*R1*p1 + p2*diff(R2,W3)*R2):
> W4 := expand(diff(R1,W4)*R1*p1 + p2*diff(R2,W4)*R2):
> M1 := expand(diff(R1,M1)*R1*p1 + p2*diff(R2,M1)*R2):
> M2 := expand(diff(R1,M2)*R1*p1 + p2*diff(R2,M2)*R2):
> M3 := expand(diff(R1,M3)*R1*p1 + p2*diff(R2,M3)*R2):
> M4 := expand(diff(R1,M4)*R1*p1 + p2*diff(R2,M4)*R2):

Create vector to loop through for taking coeffs
> unknowns := [W1, W2, W3, W4, M1, M2, M3, M4]:

Looping over all variables to get the equations from above
> results := Vector(8):
> for i from 1 to 8 do:
    unknown := unknowns[i]:
    results[i] := expand(diff(R1,unknown)*R1*p1 + p2*diff(R2,unknown)*R2):
    end do:
> results[1]:

Define the shape functions
> N1(x) := 1 - 3*(x/l)**2 + 2*(x/l)**3:
> N2(x) := x - 2*l*(x/l)**2 + l*(x/l)**3:
> N3(x) := 3*(x/l)**2 - 2*(x/l)**3:
> N4(x) := -l*(x/l)**2 + l*(x/l)**3:

Double loop to get entries of K matrix
(which consists of getting per row the equation as defined above, but now an extra loop which takes a specific coefficient and performs the integration)
> K := Matrix(8,8):
> for i from 1 to 8 do:
    result := expand(diff(R1,unknowns[i])*R1*p1 + p2*diff(R2,unknowns[i])*R2):
    for j from 1 to 8 do:
    K[i,j] := simplify(int(coeff(result,unknowns[j]),x=0..l))
    end do:
    end do:
> for ii from 1 to 8 do:
    expand(K[ii,8])
    end do:
>
> F := Vector(8):
> for i from 1 to 8 do:
    result := expand(diff(R1,unknowns[i])*R1*p1 + p2*diff(R2,unknowns[i])*R2):
    F[i] := p*simplify(int(coeff(result,p),x=0..l))
    end do:
```

$$K = \begin{bmatrix} K_{11} & K_{12} \\ K_{21} & K_{22} \end{bmatrix}$$

$$K_{11} = \begin{bmatrix} \frac{12EI^2}{l^7} + \frac{6V^2c^2}{5l} + Vck + \frac{13k^2l}{35} & \frac{6EI^2}{l^6} + \frac{V^2c^2}{10} + \frac{11k^2l^2}{210} & -\frac{12EI^2}{l^7} - \frac{6V^2c^2}{5l} + \frac{9k^2l}{70} & \frac{6EI^2}{l^6} + \frac{V^2c^2}{10} - \frac{13k^2l^2}{420} \\ \frac{6EI^2}{l^6} + \frac{V^2c^2}{10} + \frac{11k^2l^2}{210} & \frac{4EI^2}{l^5} + \frac{2V^2c^2l}{15} + \frac{k^2l^3}{105} & -\frac{6EI^2}{l^6} - \frac{V^2c^2}{10} + \frac{13k^2l^2}{420} & \frac{2EI^2}{l^5} - \frac{V^2c^2l}{30} - \frac{k^2l^3}{140} \\ -\frac{12EI^2}{l^7} - \frac{6V^2c^2}{5l} + \frac{9k^2l}{70} & -\frac{6EI^2}{l^6} - \frac{V^2c^2}{10} + \frac{13k^2l^2}{420} & \frac{12EI^2}{l^7} + \frac{6V^2c^2}{5l} - Vck + \frac{13k^2l}{35} & -\frac{6EI^2}{l^6} - \frac{V^2c^2}{10} - \frac{11k^2l^2}{210} \\ \frac{6EI^2}{l^6} + \frac{V^2c^2}{10} - \frac{13k^2l^2}{420} & \frac{2EI^2}{l^5} - \frac{V^2c^2l}{30} - \frac{k^2l^3}{140} & -\frac{6EI^2}{l^6} - \frac{V^2c^2}{10} - \frac{11k^2l^2}{210} & \frac{4EI^2}{l^5} + \frac{2V^2c^2l}{15} + \frac{k^2l^3}{105} \end{bmatrix}$$

$$K_{21} = \begin{bmatrix} -\frac{6EI}{5l^5} + \frac{6k}{5l} - \frac{V^3cm}{2EI} - \frac{13V^2klm}{35EI} & -\frac{11EI}{10l^4} - \frac{Vc}{l} + \frac{k}{10} + \frac{V^3clm}{10EI} - \frac{11V^2kl^2m}{210EI} & \frac{6EI}{5l^5} - \frac{6k}{5l} + \frac{V^3cm}{2EI} - \frac{9V^2klm}{70EI} & -\frac{EI}{10l^4} + \frac{Vc}{l} + \frac{k}{10} - \frac{V^3clm}{10EI} + \frac{13V^2kl^2m}{420EI} \\ \frac{6EI}{5l^5} - \frac{6k}{5l} + \frac{V^3cm}{2EI} - \frac{9V^2klm}{70EI} & \frac{EI}{10l^4} - \frac{Vc}{l} - \frac{k}{10} + \frac{V^3clm}{10EI} - \frac{13V^2kl^2m}{420EI} & -\frac{6EI}{5l^5} + \frac{6k}{5l} + \frac{V^3cm}{2EI} - \frac{13V^2klm}{35EI} & \frac{11EI}{10l^4} - \frac{Vc}{l} - \frac{k}{10} + \frac{V^3clm}{10EI} + \frac{11V^2kl^2m}{210EI} \\ -\frac{6EI}{5l^5} + \frac{6k}{5l} - \frac{V^3cm}{2EI} - \frac{13V^2klm}{35EI} & -\frac{11EI}{10l^4} - \frac{Vc}{l} + \frac{k}{10} + \frac{V^3clm}{10EI} - \frac{11V^2kl^2m}{210EI} & \frac{6EI}{5l^5} - \frac{6k}{5l} + \frac{V^3cm}{2EI} - \frac{9V^2klm}{70EI} & -\frac{EI}{10l^4} + \frac{Vc}{l} + \frac{k}{10} - \frac{V^3clm}{10EI} + \frac{13V^2kl^2m}{420EI} \\ -\frac{EI}{10l^4} + \frac{Vc}{l} + \frac{11k}{10} - \frac{V^3clm}{10EI} - \frac{11V^2kl^2m}{210EI} & -\frac{2EI}{15l^3} - \frac{Vc}{2} + \frac{2kl}{15} - \frac{V^2kl^3m}{105EI} & \frac{EI}{10l^4} - \frac{Vc}{l} - \frac{k}{10} + \frac{V^3clm}{10EI} - \frac{13V^2kl^2m}{420EI} & \frac{EI}{30l^3} + \frac{Vc}{2} - \frac{kl}{30} - \frac{V^3cl^2m}{60EI} + \frac{V^2kl^3m}{140EI} \end{bmatrix}$$

$$K_{12} = \begin{bmatrix} -\frac{6EI}{5l^5} + \frac{6k}{5l} - \frac{V^3cm}{2EI} - \frac{13V^2klm}{35EI} & -\frac{EI}{10l^4} + \frac{Vc}{l} + \frac{11k}{10} - \frac{V^3clm}{10EI} - \frac{11V^2kl^2m}{210EI} & \frac{6EI}{5l^5} - \frac{6k}{5l} - \frac{V^3cm}{2EI} - \frac{9V^2klm}{70EI} & -\frac{EI}{10l^4} - \frac{Vc}{l} + \frac{k}{10} + \frac{V^3clm}{10EI} + \frac{13V^2kl^2m}{420EI} \\ \frac{6EI}{5l^5} - \frac{6k}{5l} + \frac{V^3cm}{2EI} - \frac{9V^2klm}{70EI} & \frac{EI}{10l^4} - \frac{Vc}{l} - \frac{k}{10} + \frac{V^3clm}{10EI} - \frac{13V^2kl^2m}{420EI} & -\frac{6EI}{5l^5} + \frac{6k}{5l} + \frac{V^3cm}{2EI} - \frac{13V^2klm}{35EI} & \frac{11EI}{10l^4} - \frac{Vc}{l} - \frac{k}{10} + \frac{V^3clm}{10EI} + \frac{11V^2kl^2m}{210EI} \\ -\frac{12EI^2}{l^7} - \frac{6V^2c^2}{5l} + \frac{9k^2l}{70} & -\frac{6EI^2}{l^6} - \frac{V^2c^2}{10} + \frac{13k^2l^2}{420} & \frac{12EI^2}{l^7} + \frac{6V^2c^2}{5l} - Vck + \frac{13k^2l}{35} & -\frac{6EI^2}{l^6} - \frac{V^2c^2}{10} - \frac{11k^2l^2}{210} \\ -\frac{12EI^2}{l^7} - \frac{6V^2c^2}{5l} + \frac{9k^2l}{70} & -\frac{6EI^2}{l^6} - \frac{V^2c^2}{10} + \frac{13k^2l^2}{420} & \frac{12EI^2}{l^7} + \frac{6V^2c^2}{5l} - Vck + \frac{13k^2l}{35} & -\frac{6EI^2}{l^6} - \frac{V^2c^2}{10} - \frac{11k^2l^2}{210} \end{bmatrix}$$

$$K_{22} = \begin{bmatrix} \frac{433}{35l^3} - \frac{12V^2m}{5EIl} + \frac{13V^4lm^2}{35EI^2} & \frac{1271}{210l^2} - \frac{6V^2m}{5EI} + \frac{11V^4l^2m^2}{210EI^2} & -\frac{831}{70l^3} + \frac{12V^2m}{5EIl} + \frac{9V^4lm^2}{70EI^2} & \frac{2507}{420l^2} - \frac{V^2m}{5EI} - \frac{13V^4l^2m^2}{420EI^2} \\ \frac{1271}{210l^2} - \frac{6V^2m}{5EI} + \frac{11V^4l^2m^2}{210EI^2} & \frac{421}{105l} - \frac{4V^2lm}{15EI} + \frac{V^4l^3m^2}{105EI^2} & -\frac{2507}{420l^2} + \frac{V^2m}{5EI} + \frac{13V^4l^2m^2}{420EI^2} & \frac{279}{140l} + \frac{V^2lm}{15EI} - \frac{V^4l^3m^2}{140EI^2} \\ -\frac{831}{70l^3} + \frac{12V^2m}{5EIl} + \frac{9V^4lm^2}{70EI^2} & \frac{2507}{420l^2} - \frac{V^2m}{5EI} - \frac{13V^4l^2m^2}{420EI^2} & \frac{433}{35l^3} - \frac{12V^2m}{5EIl} + \frac{13V^4lm^2}{35EI^2} & -\frac{1271}{210l^2} + \frac{6V^2m}{5EI} - \frac{11V^4l^2m^2}{210EI^2} \\ \frac{1271}{210l^2} - \frac{6V^2m}{5EI} + \frac{11V^4l^2m^2}{210EI^2} & \frac{421}{105l} - \frac{4V^2lm}{15EI} + \frac{V^4l^3m^2}{105EI^2} & -\frac{2507}{420l^2} + \frac{V^2m}{5EI} + \frac{13V^4l^2m^2}{420EI^2} & \frac{279}{140l} + \frac{V^2lm}{15EI} - \frac{V^4l^3m^2}{140EI^2} \end{bmatrix}$$

$$F = \begin{bmatrix} p\left(-\frac{kl}{2} - cv\right) \\ -\frac{pkl^2}{12} \\ p\left(-\frac{kl}{2} + cv\right) \\ \frac{pkl^2}{12} \\ \frac{plmv^2}{2EI} \\ \frac{p\left(mv^2l^2 - 12EI\right)}{12EI} \\ \frac{plmv^2}{2EI} \\ \frac{p\left(-mv^2l^2 + 12EI\right)}{12EI} \end{bmatrix}$$

# C Parametric Study Results

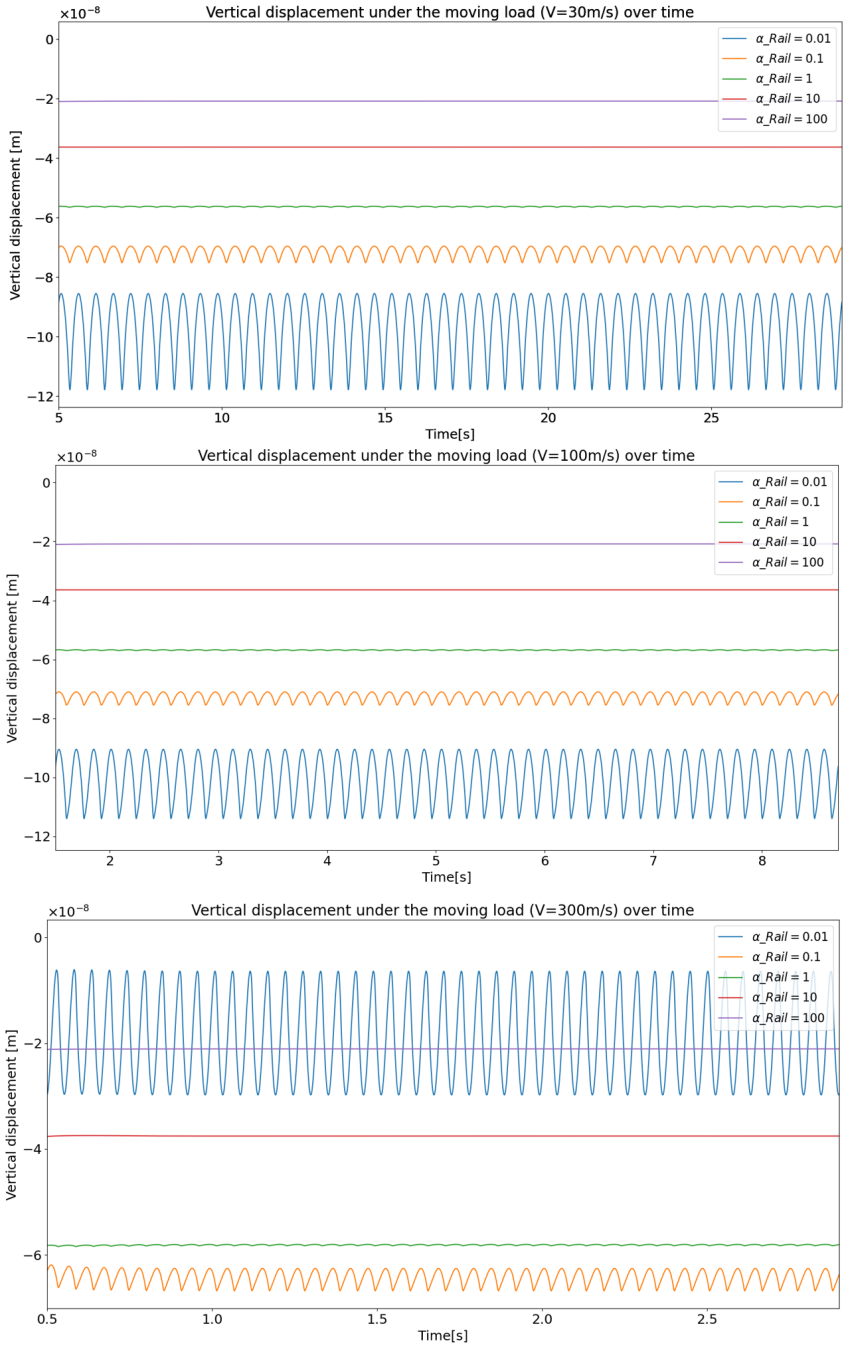


Figure 1: Different bending stiffnesses of the rail with respect to the initial bending stiffness of the tube

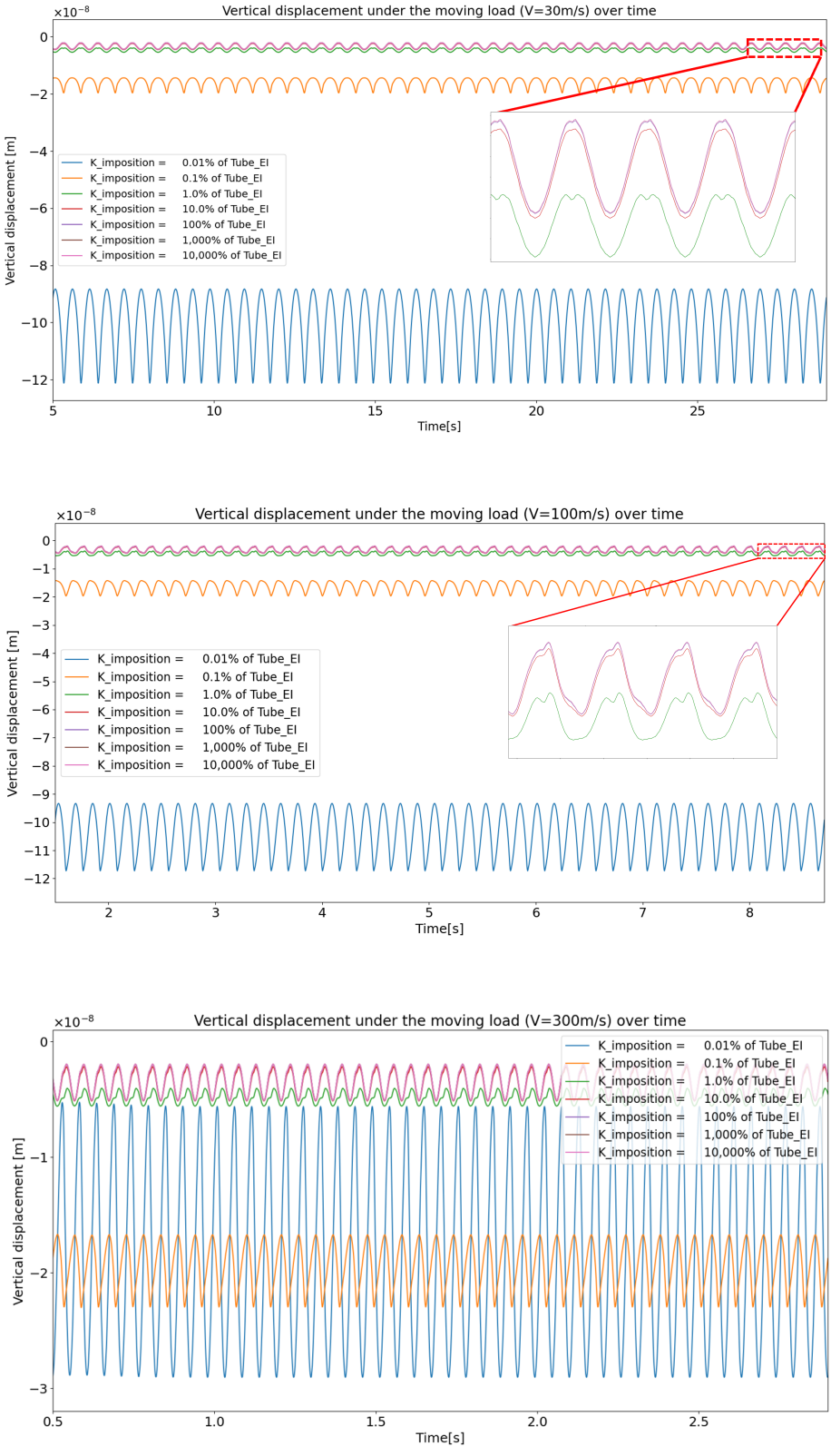


Figure 2: Vertical stiffnesses of imposition spring with respect to the initial bending stiffness of the tube

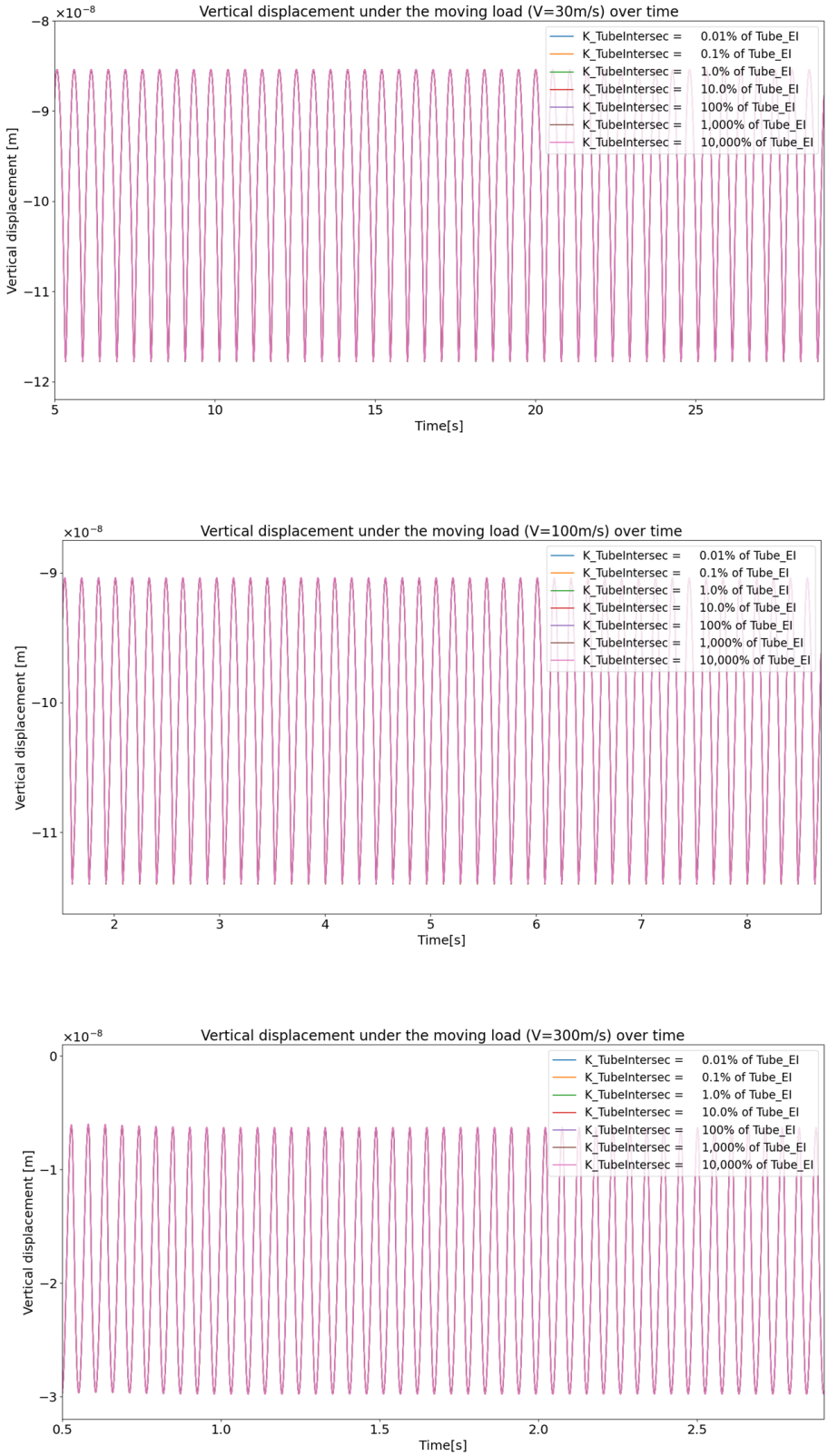


Figure 3: Vertical stiffnesses of tube intersection spring with respect to the tube's initial bending stiffness

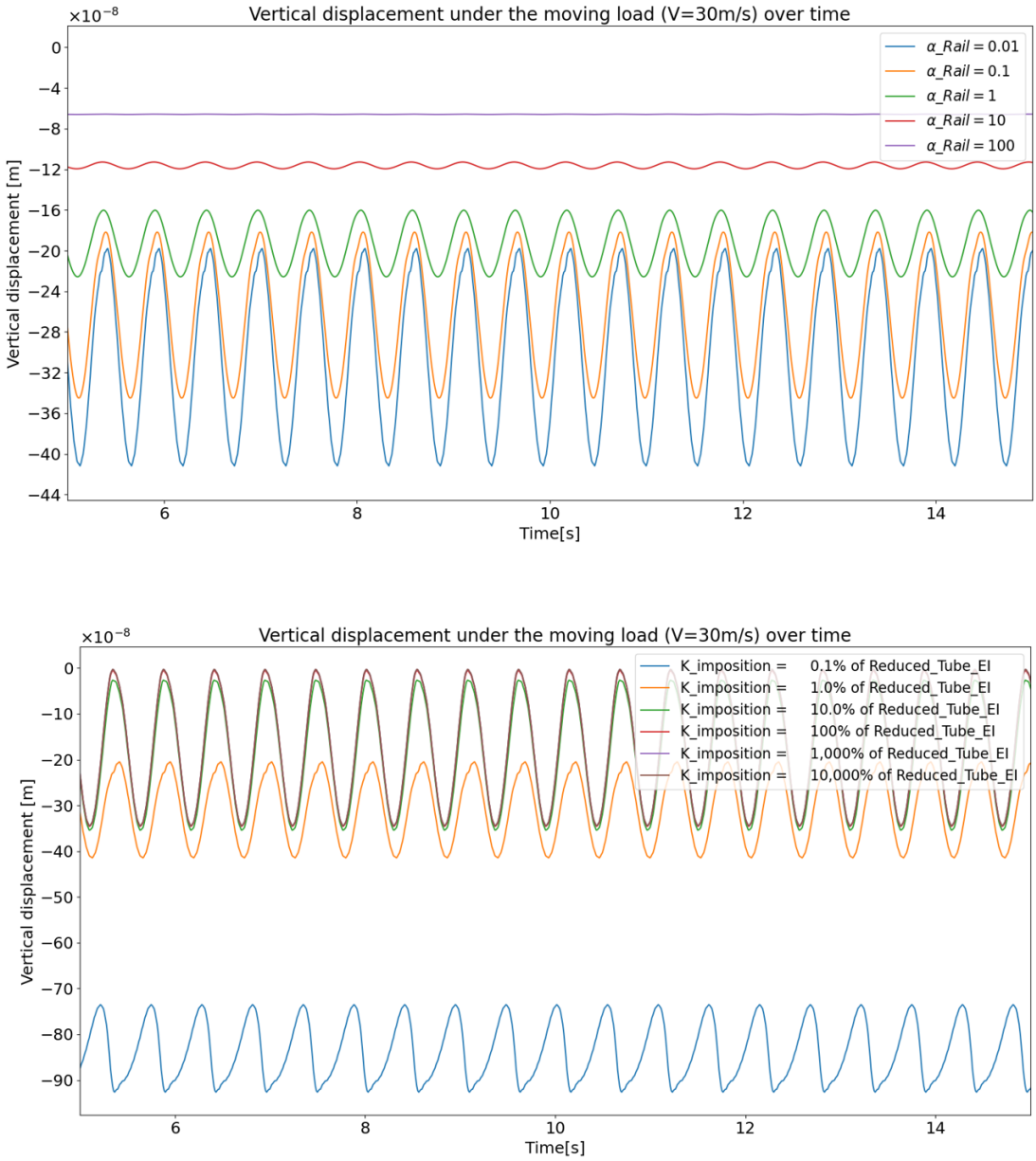


Figure 4: Vertical stiffnesses with respect to the reduced bending stiffness of the tube

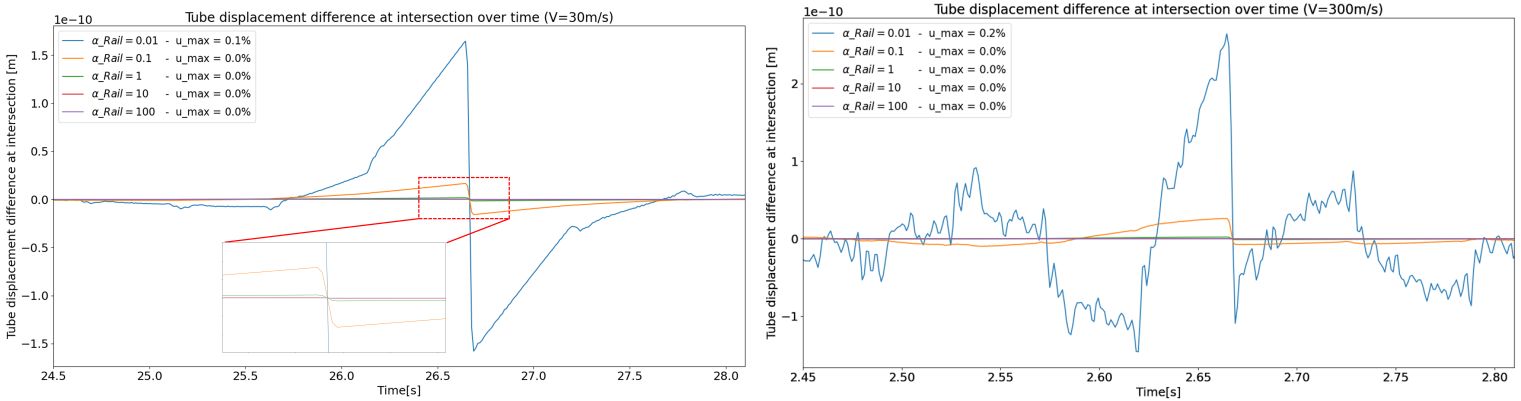


Figure 5: Tube displacement difference for different rail bending stiffnesses

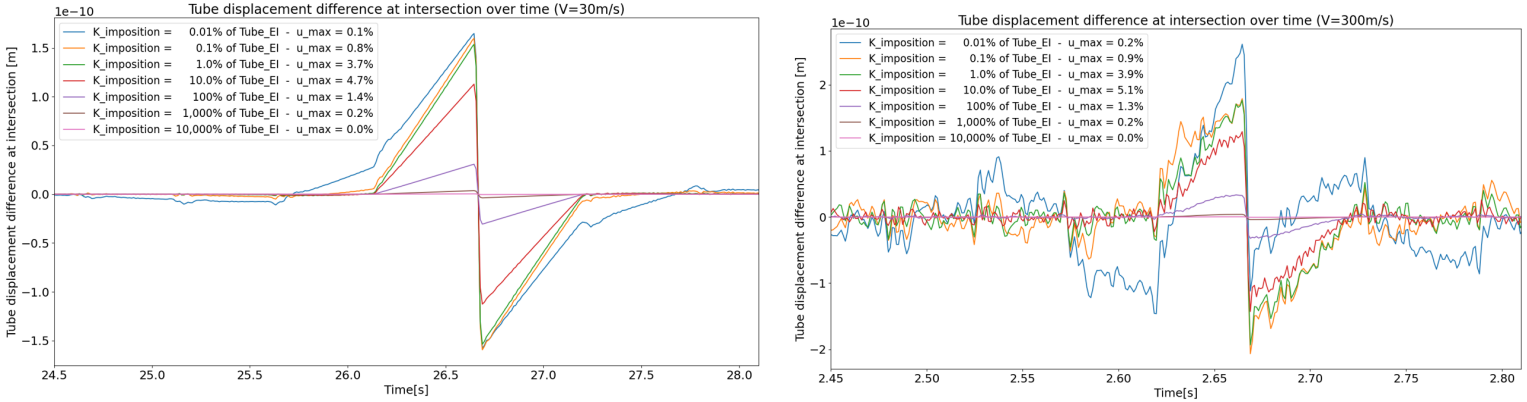


Figure 6: Tube displacement difference for different imposition stiffnesses

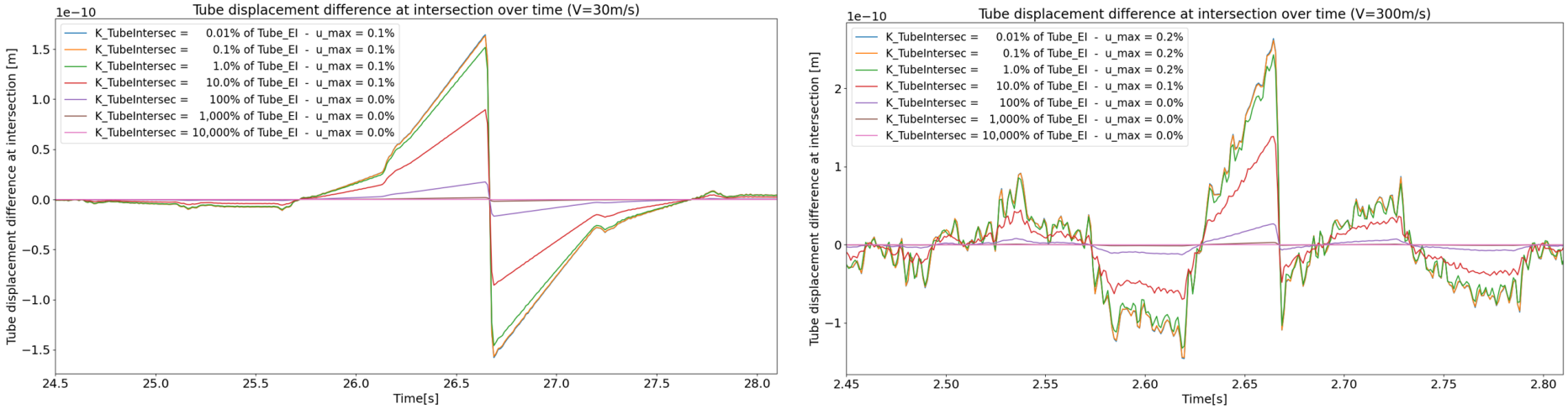


Figure 7: Tube displacement difference for different vertical stiffnesses at the tube intersection

# D Soil Properties

The key mechanical properties of soil are provided in the table below with a detailed explanation of their relations and roles in soil behaviour [46].

| **Property** | **Symbol** | **Definition** | **Formula** | **Units** |
|---|---|---|---|---|
| Modulus of Elasticity | $E$ | The stiffness of soil under axial stress. | $E = \frac{\sigma}{\varepsilon}$ | Pa |
| Poisson's Ratio | $\nu$ | Ratio of lateral strain to axial strain in response to loading. | $\nu = \frac{\varepsilon_{\text{lat}}}{\varepsilon_{\text{axial}}}$ | - |
| Shear Modulus | $G$ | Soil's resistance to shear deformation. | $G = \frac{E}{2(1+\nu)}$ | Pa |
| Bulk Modulus | $K$ | Soil's resistance to uniform compression. | $K = \frac{E}{3(1-2\nu)}$ | Pa |
| Subgrade Modulus | $k$ | The stiffness of soil in supporting loads, particularly in foundations. | $k = \frac{E}{(1-\nu^2)B}$ | Pa/m |
| Shear Strength | $\tau$ | The maximum resistance of soil to shear stress. | $\tau = c + \sigma' \tan\phi$ | Pa |
| Bearing Capacity | $q$ | Maximum load per unit area the soil can support without failure. | $q = cN_c + \sigma' N_q + 0.5\rho g B N_\gamma$ | Pa |

Table 1: Overview of the mechanical soil properties

The measurements of stress ($\sigma$) and strain ($\epsilon$) are crucial for determining the key mechanical properties. The stress and strain are calculated in field tests or in the laboratory. The triaxial test is commonly performed to obtain stress and strain data. The test measures axial and lateral deformation of soil samples when subjected to loads. From this data, two critical mechanical properties, the Young's modulus ($E$) and Poisson's ratio ($\nu$), are calculated. These two properties, once determined, are essential for further calculations because the shear modulus ($G$), the bulk modulus ($K$) and the subgrade modulus $k$ can be derived, respectively show the resistance to shear deformation, shear compression and the soil stiffness. Where the width or diameter of the loaded area is represented with the variable $B$. In addition to the triaxial tests, shear tests are executed to gather the cohesion ($c$) and friction angle ($\phi$) of the soil sample. These parameters give the shear strength ($\tau$) calculated with the effective stress ($\sigma' = \sigma - u$), where the pore water pressure is represented by $u$. The bearing capacity of the soil ($q$) can be calculated by Terzaghi's Equation [47]. The first two terms of the equation address the problem of the determination of the failure load of a half-plane carrying a distributed load on the surface [48]. The equation is extended with a third term to take into various refinements, such as an inclined load and the influence of the shape of the load. Where $\rho$, $g$ and $B$ respectively represent the density, gravitational constant and the load width. The coefficient $N_\gamma$ does not have a general expression, various suggestions have been made based on theoretical analysis and experimental evidence. With these parameters, engineers can predict the soil performance under real-world conditions, such as foundation loading or other forces. This makes the tests and properties essential for ensuring the stability and safety of structures built on the soil layers.